Optical properties of Colloidal PbTe and its Oriented Attachment

MASTERTHESIS BY JUR DE WIT

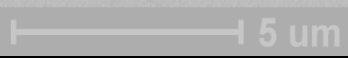

Supervisors: Joep Peters and prof. Daniël Vanmaekelbergh
CONDENSED MATTER & INTERFACES | UTRECHT UNIVERSITY

The front page background is a transmission electron microscope image and illustrates drying patterns as observed in the microscope.

Abstract. PbTe nanocrystals (NCs) ranging in size from 3.5 to 7 nm have been synthesized using the hot-injection method. Based on these particles, a relation between the first absorption peak position and NC size has been established. Inductively coupled plasma optical emission spectrometry (ICP-OES) and energy dispersive x-ray spectroscopy (EDX) were combined with UV-vis-NIR spectroscopy to determine the NC concentration and molar absorption coefficient (ε). At 3.1 eV, ε scales with NC volume and is size independent. At the bandgap, ε is size-dependent because of quantum confinement effects. Different sizes of PbTe have been used for oriented attachment procedures. NCs of 5.74 nm are best suited for square oriented attachment procedures. Other attachment parameters that were investigated are: solvation of Pb-oleate in ethylene glycol, ligand density and size dispersion.

Contents

Introduction

Semiconductor nanocrystals are known to have been applied as far back as antiquity, where it was used to dye hair. In this specific case, the ancient Egyptians got black hair because Lead Sulfide (PbS) nanocrystals (NCs) were ingrained in hair strands after administering a paste containing PbS[1]. Some 3000 years later, there is a rich and diverse scientific community studying these class of materials due to the many possibilities it offers. This scientific interest originates in large part from the influence of NC size on spectroscopic and thermodynamic characteristics.

The effect of NC size on electric and optical properties is called quantum confinement (figure 1). Bulk semiconductor materials have a physical property called the Bohr exciton radius, which indicates the average distance between and electron and hole after excitation[2]. If the diameter of a NC is smaller than the Bohr radius, the exciton will be confined within the boundaries of the NC. Two results of the confinement are the discretization and increase of the semiconductor bandgap[3]. This larger bandgap translates to a blueshift in the emission and absorption spectrum of quantum confined semiconductor materials. Because of this effect, the tale of these materials is in a large part told by light.

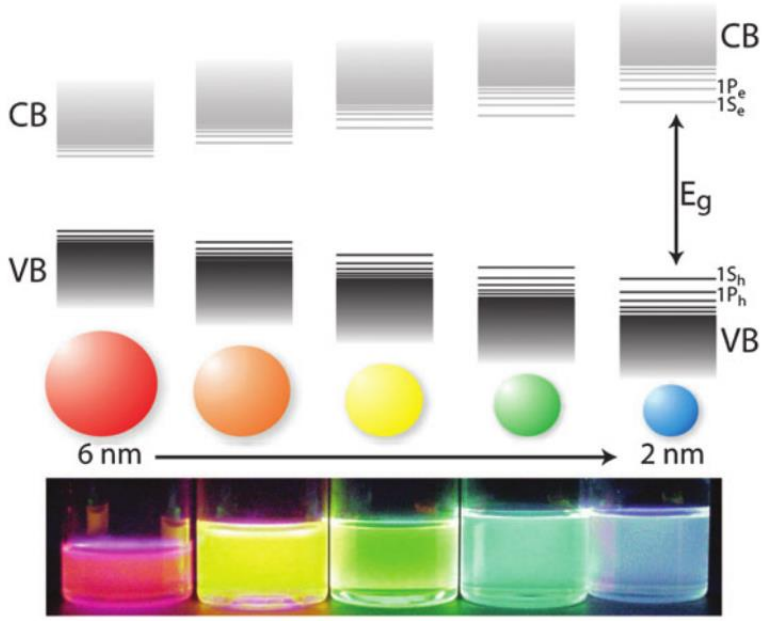

Figure 1. The image shows a schematic representation of the quantum confinement effect, as seen in CdSe NCs. In the upper part of the figure an energy diagram depicts the effect of quantum confinement on the semiconductor bandgap: with decreasing size both a discretization of energy levels and a widening of the band gap is observed. The colored solutions seen in the lower part are solutions containing differently sized NCs illuminated with UV-light. Figure adapted from Ref. [2]

The very small size of NCs also affects thermodynamic properties due to the high surface to volume ratio. The large surface area causes NCs to be inherently unstable, and the first attempts to counteract this problem were to embed the NCs in glassy matrices[4], much like Egyptian strands of hair. It was almost a decade after this initial discovery, in 1993 that a solution-processed method was developed for the synthesis of stable NCs; called the hot-injection method[5]. The novelty of this approach was threefold: firstly, the surface of the CdE (E= S, Se, Te) NCs was covered by protective ligands that kept it stable in solution. Secondly, the synthesized NCs produced homogeneously sized particles needed for effectively realising

quantum confinement effects. Thirdly, it was a relatively straightforward and easily reproducible method. These three reasons combined have made the hot-injection method a highly versatile road to manufacture a variety of nanosized structures[6–9].

With the continuous improvement of optical properties and monodispersity of NCs, a number of new applications have come within reach[10]. One of these developments is the self-assembly of separate NCs into larger crystalline structures, much like Lego® blocks[11]. An exciting aspect of these structures is that the non-classical crystallization pathway makes that its characteristics are dependent on the building blocks[12]. It may also provide a cost-effective and flexible way of developing bottom-up approaches to materials that nowadays are produced with relatively expensive etching techniques. These considerations established the usefulness of self-assembly, but also created a new problem: understanding and effectively governing the complex dynamics that underlie this process.

These considerations have been researched in the self-assembly and subsequent oriented attachment (OA) of PbSe NCs into larger 2D superstructures[11]. Inspired by the intriguing but elusive optoelectronic properties of graphene, there have been several reports on honeycomb oriented 2D-superlattices[13–15]. Tight-binding calculations on this class of materials have indicated that the band structure of such superstructures show a strong resemblance to that of graphene. However, the semi-conductor nature of the building blocks of such a material, combined with relativistic spin-orbit coupling effects result in a non-trivial band structure with multiple Dirac-cones at reachable bandgap energies[16].

In the family of lead chalcogenide semiconductors, the above effects are even more pronounced in the heavy lead telluride (PbTe). The more reactive and oxygen-sensitive PbTe has received less attention than its siblings have. There have been reports on the application of PbTe in photovoltaics[17] and thermoelectric devices[18]. But in comparison with PbS and PbSe, working with PbTe proves challenging because there is no straightforward way to accurately determine NC size and concentration. This research will therefore focus on the synthesis and opto-electronic properties of PbTe, as to make it more user-friendly. The other focal point will be the post-synthesis treatments cation exchange and oriented attachment.

Theory

Nucleation and growth

Thermodynamic approach

A common model used to describe the formation of colloidal metal chalcogenide NCs from monomers is the Classical Nucleation Theory (CNT)[19] . According to this model, nuclei, or clusters, form a template for the final material, from which further growth is enabled. The formation process can be considered from a free energy perspective: the free energy of a nucleus consists of a volume part and a surface part. They compete with each other in the sense that the surface energy increases the Gibbs free energy (ΔG), while volume energy decreases ΔG. By looking at the total free energy as a result of these two energies, the following equation can be applied:

$$\Delta G_{total} = \Delta G_{surface} + \Delta G_{volume} = 4\pi r^2\gamma - \frac{4}{3}\pi r^3 \frac{k_B T ln(S)}{v} \quad (1)$$

Where r is the radius of the nuclei, k_B is the Boltzmann constant, T is temperature, γ is the surface tension, v is the molar volume of the semiconductor and S is the supersaturation of the solution.

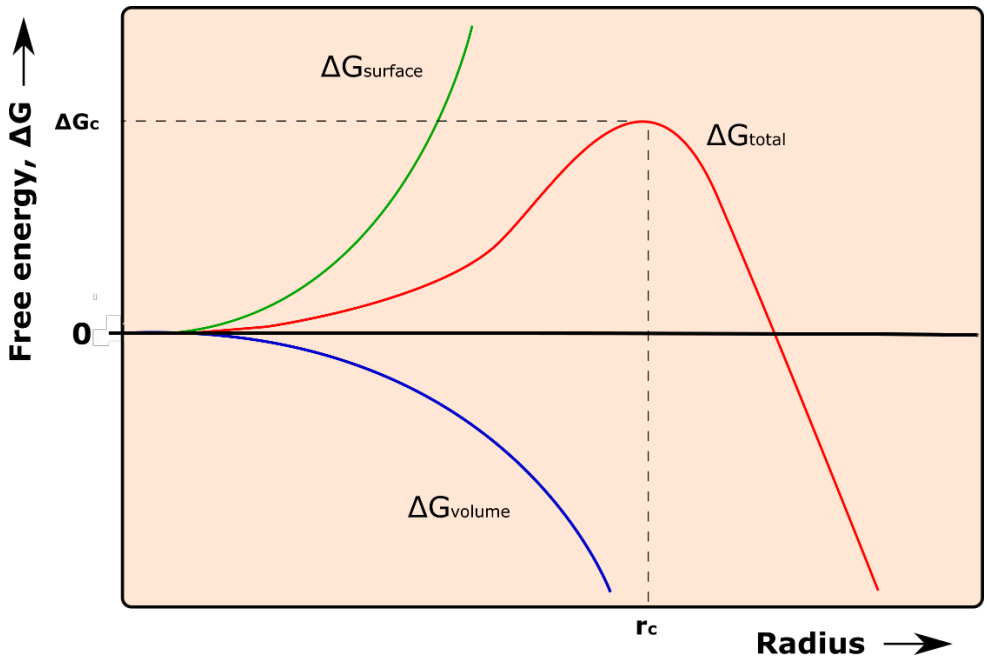

Figure 2. The green line indicates the positive Gibbs free energy as a result of the surface of the NC. This factor will always be positive because the surface is inherently less stable than the interior of a NC. It scales with r^2. The blue line describes the decrease in Gibbs free energy as a result of the increasing volume with ratio and scales with r^3. The total free energy, as described by the red line is a combination of the previous two and reaches a maximum at the critical radius. Once a NC surpassed this size, it will be energetically favorable to become larger, as demonstrated by the downward slope of the total free energy.

Since the volume factor scales with r^3 and the surface factor with r^2, the cluster eventually reaches a critical point at which it is will not re-dissolve in solution. This size is called the critical radius of a cluster, which can be determined by equating the derivative of the Gibbs free energy, dΔG/dt to 0. The resulting equation is an expression for the critical radius of a nucleus:

$$r_{critical} = \frac{2\gamma v}{k_B T ln(S)} \quad (2)$$

The corresponding critical radius of the nucleus indicates the size of the particle at which it will not redissolve, but keeps growing. In figure 1, the dashed line depicts the maximum of the total free energy.

Kinetic approach

The mechanism proposed by La Mer divides the formation process of NCs into three different categories and is applicable to the hot-injection method (figure 2)[19,20]. (I) The injection of one of the two precursors almost instantly increases monomer concentration in solution until it reaches the critical concentration. (II) Once the critical concentration is reached, the dynamic equilibrium is shifted from redissolving to nucleus formation. Only the clusters that have a size larger than the critical radius will keep growing in this case. Once a discrete amount of nuclei is formed and the temperature and monomer concentration are sufficiently low, the growth phase begins (III). In the growing stage, monomers and dimers still in solution will attach to existing nuclei through a diffusion-limited process[21]. After some time the concentration will be sufficiently low for the equilibrium to be completely shifted towards the NCs [22].

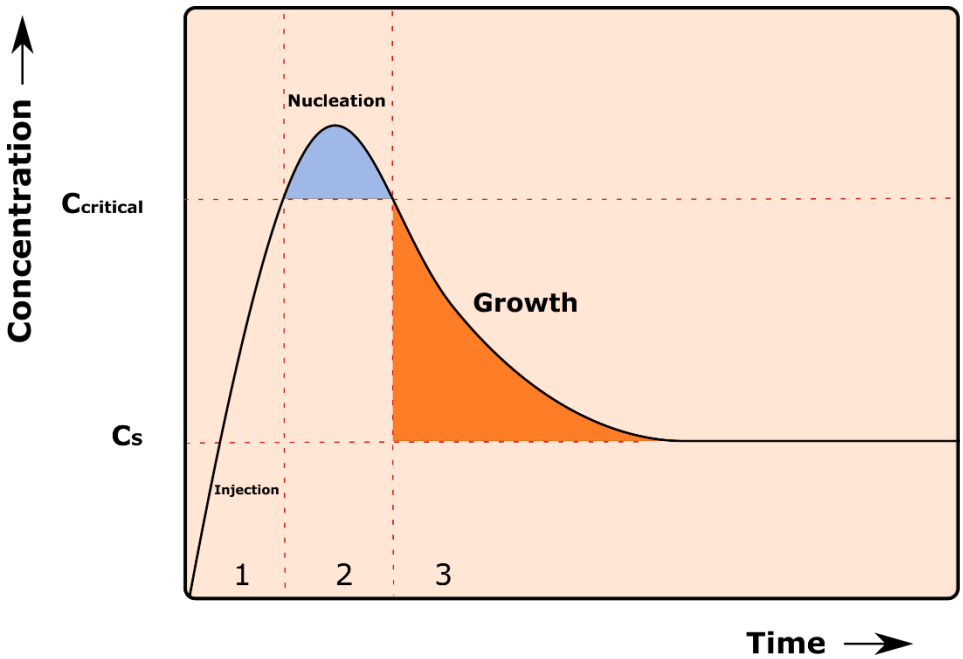

Figure 3. The above La Mer diagram describes the three stages of NC formation. (1) A strong increase in concentration leads to a (2) nucleation phase, which results in a concentration decrease. After the "seeds" are formed, more monomers attach to the surface to increase the NC size in phase (3).

During this three-step process it is crucial that the nucleation phase is short, because this will result in the formation of many roughly equally sized nuclei. If the nucleation phase takes longer due to e.g. slow injection, a polydisperse set of nuclei is formed. During the growth phase, these nuclei will then grow into differently sized NCs. In case of a monodisperse set of nuclei with $r > r_c$, size focusing will occur. For a system with a wide distribution of particle sizes, Ostwald ripening may affect the final distribution[21]. This is a process where smaller particles re-dissolve because of their high surface to volume ratio. Larger particles remain stable and

will grow at the expense of the re-dissolved smaller particles, leading to large particles and a wide size distribution[23].

Role of ligands

During and after synthesis, ligands play a crucial role in the formation and stability of NCs. In the formation process, ligands control the nucleation and growth kinetics of NCs. For example, varying ligand size, concentration and ratio can make the difference between quantum dots, nanorods or nanoplates[24]. In solution, a stabilizing layer of ligands is formed around the NCs and prevents them from agglomerating (figure 3). Which type is used depends on the solvent: polar solvents require electrical stabilization, while apolar solvents demand steric hindrance in the form of (long) hydrocarbons[24]. Furthermore, the capping layer around the NC passivates dangling bonds and thereby increases photoluminescence[25] A commonly used ligand is applied to PbTe: two oleate molecules bound to Pb provide the steric hindrance needed for colloidal stability and neutralizing Vanderwaalsforces[26]. An important result of this capping layer is a surface excess of Pb on the NC[27]. The way oleate ligands cover the Pb-rich surface is called an Z-type ligand system, because the $Pb(oleate)_2$ complex effectively acts as one ligand[28].

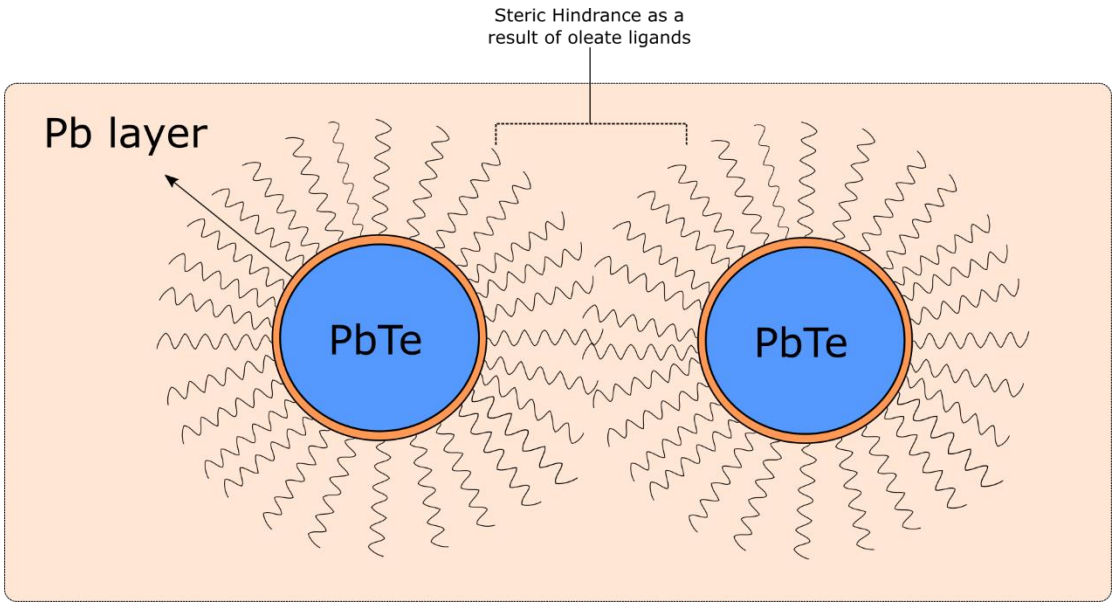

Figure 4. Schematic representation of PbTe NCs capped by Pb-oleate ligands. When the NCs are dissolved, the oleate carbon chains prevent the particles from agglomerating through steric hindrance. The orange, outer layer of the NCs is a result of the oleate exclusively binding to Pb on the NC surface.

Quantifying light absorption by NCs

Sizing curve

As described above, it is a well-established fact that light absorption and emission of NCs is dependent on the size of NCs. Theoretical research combined with experimental data has also demonstrated there to be a relation between energy gap and NC size[29]. Therefore, the position of the first excitonic peak has been used extensively as a measure for the size of metal chalcogenide NCs like CdX (X=S, Se, Te) and PbX (X=S, Se) [30–33]. By plotting the peak position of the first optical transition in eV to the size of the NC, one can determine an empirical fit between these variables. A major benefit of such a fit is that size determinations of NCs do not depend solely on the laborious and unreliable manual counting of particles on TEM images.

A starting point for such a sizing curve is the bandgap energy of the bulk material, since with increasing size this value will be approached. Some debate exists about the exact bandgap value of PbTe, since values vary between 0.28-0.36 ev[34,35], probably a result of temperature influences on bandgap measurements. In a recent paper however, an experimental linear relationship has been established between the PbTe bandgap energy and temperature[36]. The following equation has been determined for temperatures under 400K and is filled in with 293K:

$$E_g = 0.19 + (0.42 * 10^{-3}) * 293K = 0.313\ eV \tag{3}$$

NC Concentration

The concentration can be determined by combining two separate techniques. An inductively coupled plasma optical emission spectrometer (ICP-OES) can be used to calculate the concentration of NCs. Furthermore, the metal chalcogenide ratio R is also important in this case, since there is a metal-ligand complex around the NCs[32]. This data is usually acquired with energy dispersive x-ray spectroscopy (EDX) or Rutherford backscattering (RS)[37]. So, the total number of atoms N for a spherical NC equals:

$$N = \frac{4\pi}{3}\left(\frac{d}{a}\right)^3 \tag{4}$$

Where a is the lattice parameter and d is the particle diameter, both in nm. This diameter is uncorrected for the uneven ratio R between metal and chalcogenide per NC, which is taken into account in the formula used to calculate the NC concentration[32]:

$$[PbTe] = \frac{1}{N}\frac{1+R}{R}C_M \tag{5}$$

Where C_M is the Pb concentration in mol/L, as derived from the ICP-OES measurements.

Molar absorption coefficient

The absorption spectrum of NCs also contains information about the molar concentration of NCs in solution. When a beam of light is send through a cuvette containing colloidal NCs, some of the light will be absorbed. The relation between light absorption A, pathlength L, molar concentration c and the molar absorption coefficient ε is expressed by the Lambert-Beer law:

$$A = \varepsilon c L \tag{6}$$

In this equation there are two unknowns, namely the molar absorption coefficient and NC concentration. Once the molar absorption coefficient of NCs is known for different sizes at a specific wavelength, it is relatively straightforward to calculate NC concentration with the above formula.

To this date, the molar absorption coefficient has been determined at two different regions of the spectrum. The first method determines the molar absorption coefficient at the band gap by integrating the area underneath the low energy half of the absorption peak[30]. The second method is based on the argument that absorption at energies far above the bandgap, quantum confinement effects do not play a significant role for lead chalcogenides[37]. Both methods will be discussed in the coming section.

Molar absorption coefficient at band gap

The energy integrated molar absorption coefficient as a means of determining NC concentration has been applied for various materials[30–32,38]. Depending on the material, only the first half of the absorption peak is used because it is not convoluted with higher energy excitons. A benefit of the resulting energy integrated molar absorption coefficient is that it does not have to be calibrated for differences in size dispersions between samples[30]. However, small shifts in the first absorption peak due to broad size dispersions can influence the such measurements[32].

Molar absorption coefficient at 3.1 ev

The lack of quantum confinement effects at energies far above the bandgap paves the way for applying the same method used for calculating the absorption coefficient. It does have to be taken into account that the NCs are dispersed in another medium[37]:

$$\mu = \frac{\ln(10)\,A}{L} = \frac{4\pi\kappa_{eff}}{\lambda} \tag{7}$$

Where A is the absorption, L the optical path length, lambda the wavelength and κ_{eff} is the effective extinction coefficient. The difference between κ and κ_{eff} is a result of the NCs being dispersed in a solution with a different dielectric function.

In a feature article by Hens and Moreels in 2012, the Maxwell-Garnett mixing rule is applied to the system to correct electrical screening factors[37]. The relation between the dielectric function of the NCs and the solvent is characterized by a new composite dielectric function $\tilde{\varepsilon}_{eff}$, consisting of a real and imaginary part, $\varepsilon_{eff,R}$ and $\varepsilon_{eff,I}$ respectively. According to this model, in a sufficiently dilute solution $\varepsilon_{eff,R}$ is reduced to the dielectric function of the solvent: ε_s. The imaginary part depends on the volume fraction f of PbTe in solution and the dielectric functions of the solvent and bulk PbTe:

$$\varepsilon_{eff,I} = \frac{9\varepsilon_s^2}{|\tilde{\varepsilon}_{PbTe} + 2\varepsilon_s|^2} f\,\varepsilon_{PbTe,I} \tag{8}$$

The imaginary part can then be rewritten by using the concept of the local field factor f_{LF} and the approximation of PbTe NCs as dielectric spheres. The local field is induced because a dielectric sphere (NC) is immersed in a homogeneous (solvent) electric field. The resulting local field factor is defined as the ratio between the local electric field and the external electric field:

$$f_{LF} = \frac{3\varepsilon_s}{|\tilde{\varepsilon}_{PbTe} + 2\varepsilon_s|} \tag{9}$$

The equations (6), (7) and (8) are then combined with the definition of the effective extinction coefficient (10)[37], to find an expression for the effective absorption coefficient for PbTe NCs:

$$\kappa_{eff} = \frac{\varepsilon_{eff,I}}{2n_s} \tag{10}$$

$$\mu = \frac{2\pi}{\lambda n_s} |f_{LF}|^2 f\,\varepsilon_{PbTe,I} \tag{11}$$

Then the intrinsic absorption coefficient is found by dividing by the volume fraction f, which leads to following relation:

$$\mu_i = \frac{2\pi}{\lambda n_s} |f_{LF}|^2 \varepsilon_{PbTe,I} = \frac{\ln(10)\, A}{fL} \tag{12}$$

Now, the intrinsic absorption coefficient is related to the volume fraction of NCs dispersed in the solution and the dielectric function of bulk PbTe.

Cation exchange

Cation exchange (CE) describes the post-synthetic process where cations of the parent NC are exchanged for different cations. Due to the small size of NCs, diffusion of cations in and out of the material are less of a limiting factor than for their bulk counterparts[39]. It also provides an alternative route to materials that are difficult to obtain through direct synthesis protocols, such as HgTe[40]. Because these exchanges can be topotactic, i.e. the crystal structure and shape are retained, novel structures have come within reach[41]. By tuning the reaction conditions, CE can take place in varying degrees: from complete exchange to a range of partial exchanges[41].

The procedure of CE has been in the limelight but there is still an ongoing debate about different exchange mechanisms at play. There have been various efforts to describe into detail the kinetic and thermodynamic properties of CE and how these can be altered by changing CE parameters[40,41]. One of the most important thermodynamic parameter is the hardness of the acids and bases used, which describe the affinity of metal ions to ligands[42]. Thus, an exchange reaction is *a priori* favourable if the host cation preferably binds to the ligand in solution. Another thermodynamic factor is the lattice enthalpy: the propensity of cations to exchange is determined by the surface energy and lattice enthalpy of the original and new material[43]. All these consideration have to be taken into account if one sets out to *a priori* deterimine whether a CE reaction will be successful or not.

Kinetic considerations also have to be taken into account for CE reactions, since the cations have to diffuse through the crystal structure. The exchange reaction is initiated at the surface, after which the host cations are being forced out. Depending on the favourability of the exchange reaction, harsh or mild reaction conditions need to be applied[43]. Harsh conditions are high reaction temperatures, long reaction durations and large cation excesses. Although the addition of a large excess of cations could also impede the exchange reaction by poisoning the NC surface[40].

A demonstration of complete cation exchange from PbTe to cadmium telluride (CdTe) has not been found in literature. PbX (X=S, Se) structures on the other hand have been cation exchanged to the corresponding CdX nanocrystals and *vice versa*[44,45]. For PbTe to CdTe conversions only partial CE has been described[46]. However, they also stated that by increasing the reaction time and Cd:Pb ratio almost complete CE was obtained. The transition between Pb and Cd is difficult since the lattice enthalpy of PbTe is lower than that of CdTe[47]. Consequentially, already large Cd overdoses are used by Lambert *et al*. to realize partial cation exchange of Cd for Pb[46]. Because of the small lattice mismatch and almost identical ionic radii it likely that the original rock-salt structure can be maintained[46].

Oriented Attachment

Early oriented attachment experiments in the lead chalcogenide family focused on the growth of anisotropic structures such as nanowires and ultrathin nanosheets[48–50]. These in-solution attachment procedures relied on the addition of ligand mixtures or cosolvents, thereby creating a preferred attachment pathway through activated facets[50]. A major difficulty with these methods is control: due to the high temperature syntheses, irreversible and extremely fast oriented attachment occurs. In a more recent experiment, post-synthesis oriented attachment of separate PbSe NCs was achieved under moderate conditions[51]. Here, oriented attachment of PbSe NCs was perfromed by dropcasting a suspension on an immiscible substrate, after which the suspension was evaporated (Figure 5). By varying the temperature and NC concentration, both 1D-linear and 2D-superstructrures were obtained[51].

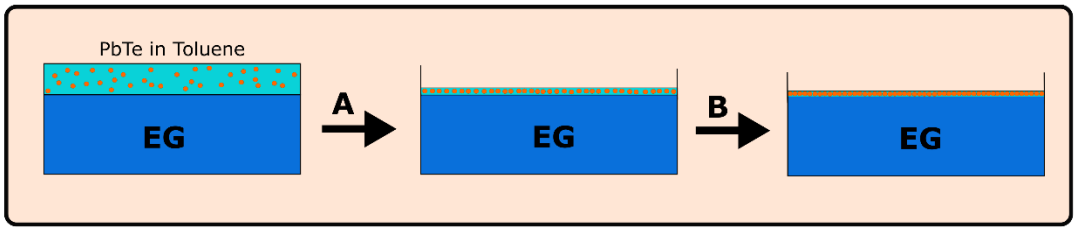

Figure 5. Schematic representation of the oriented attachment procedure described by Evers et al[51]. In the left image, PbTe NCs are dissolved in toluene and cast on top of an immiscible ethylene glycol (EG) interface. During step (A) the toluene evaporates and the concentration of PbTe NCs increases. In step B, all toluene is evaporated and the NCs form a superlattice upon the EG interface.

On the formation mechanism

The difficulty of understanding self-assembly and oriented attachment processes lie in the number of variables it depends on[52]. In the specific case of lead chalcogenide NCs, several suggestions have been proposed to improve superlattice formation. Ondry et al have shown that attachment via small {100} facets on PbTe NCs lead to large scale structures with easily removable defects[53]. They proposed that for optimal attachment pathway a high degree of control over truncation is beneficial. The propensity to attach via {100} facets is twofold: first, the checkerboard arrangement of Pb^{2+} and S^{2-} the {100} facets[54] is ideal for atomic binding between NCs[55]; second, the dense hexagonal packing on {111} facets is covered with oleate ligands[56]. Moreover, PbS ligand coverage strongly influences self-assembly: reduced ligand coverage due to additional washing leads to reduced grain sizes[52].

Square

Further research aimed at PbSe square superlattices acquired with this method have studied the formation mechanism with *in-situ* grazing incidence X-rax spectroscopy and *ex-situ* electron microscopy[57]. This approach has led to the identification of a multi-step assembly and attachment process, which starts with the formation of a hexagonal monolayer as the toluene evaporates (figure 2a). The NCs composing this monolayer are confined to the liquid-air interface and have complete rotational freedom. This continuous rotation allows the NCs to interact with other particles and find a “perfect lattice match”[58,59]. After some time, the NCs form a pseudo-hexagonal monolayer where all NCs have a {100} facet perpendicular to the liquid-air interface. Moreover, because of ligand desorption from the {100} facets and electrostatic and van der Waals interactions between {100] facets, the NC-NC distance is

reduced (figure 2b). In the final step, the orientation gradually changes from pseudo-hexagonal to square, because of the in-plane square {100} attraction. Subsequently, the NCs lose all rotational freedom and form crystalline bridges between separate NCs (figure 2c).

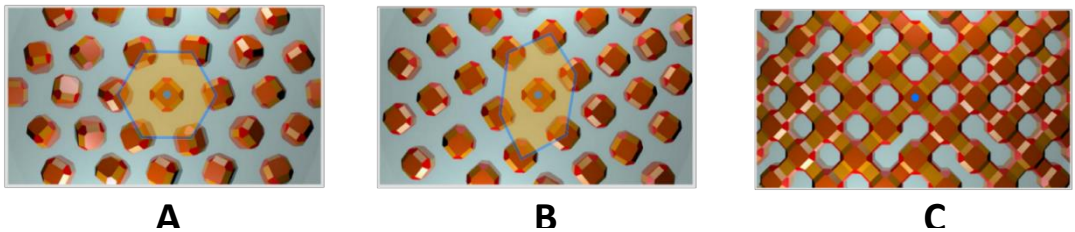

Figure 6. Schematic depiction of PbSe NCs square attachment. In figure A, the NCs form a hexagonal monolayer and have full ratotional freedom. In figure B, the {100} facet is perpendicular to the EG interface and NC-NC distance is reduced due to ligand desorption. The rotational freedom is limited and a pseudo-hexagonal monolayer is formed. In figure C the NCs have no rotational freedom and have formed crstyalline bridges between separate NCs.Adapted from Ref [5].

Honeycomb

The only experimental report to date about PbSe honeycomb structures used a similar evaporation method as described in figure 1[13]. They showed that the honeycomb geometry can be described by a silicene structure: two parallel planes consisting of NCs are attached to each other via the {100} facets in a buckled fashion. They also found elongated bond lengths between NCs, from which they concluded that considerable atomic reconfigurations are necessary to facilitate these necks. Although this structure was not analysed with *in-situ* methods, it is likely that NC self-assembly and the desorption of weakly bound {100} oleate ligands, also facilitate the formation of lattice matches[24].

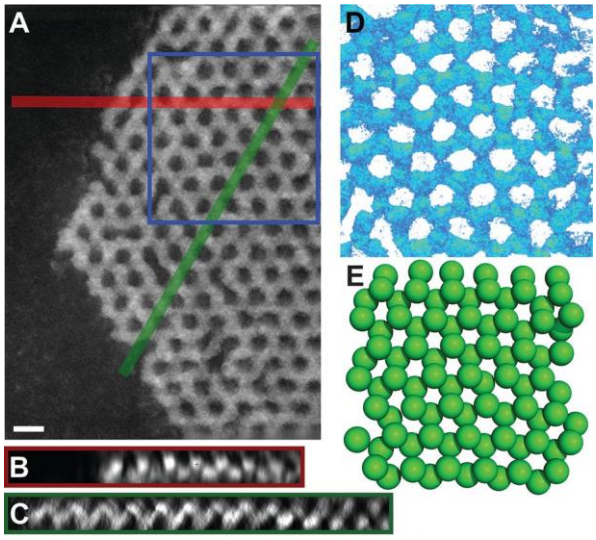

Figure 7. A is a HAADF-STEM tomography image of a PbSe honeycomb structure. Along the red and green line slices through the tomograph structure indicate the buckled orientation (B,C). In the blue box region, an isovolume rendering of the attached NCs is shown in figure D. In figure E, equally sized spheres are placed on the coordinates found by automated particle detection. Adapted from Ref. [13].

Experimental

List of chemicals

Chemical	Abbreviation	Supplier	Purity (%)	M (g/mol)	Density (g/mL)
1-Butanol (anhydrous)	BuOH	Aldrich	99.8	74.12	0.810
1-Octadecene	ODE	Aldrich	90	252.48	0.789
Acetonitrile (anhydrous)	ACN	Aldrich	99.8	41.05	0.786
Cadmium (II) acetate dihydrate	$Cd(OAc)_2$ $2H_2O$	Aldrich	≥99.99	266.53	-
Cadmium (II) oxide	CdO	Aldrich	≥99.99	128.41	-
D-chloroform	-	Aldrich	99.8	120.384	1.50
Diphenylether	DPE	Aldrich	99	170.2	1.073
Ethanol (anhydrous)	EtOH	Aldrich	99.8	46.07	0.789
Ethylene glycol (anhydrous)	EG	Aldrich	99.8	62.07	1.11
Hexane (anhydrous)	Hex	Aldrich	95	86.18	0.655
Hydrochloric acid, 37%	HCL	Aldrich	37	36.36	1.2
Lead acetate trihydrate	$Pb(OAC)_2$ $3H_2O$	Aldrich	≥99.99	379.33	-
Methanol	MeOH	Aldrich	99.8	32.04	0.792
Nitric acid (65%)	HNO_3	VWR	65	63.01	1.39
Oleic acid	OA	Aldrich	90	282.46	0.895
Tellurium (200 mesh)	Te	Aldrich	99.9	127.60	-
Tellurium (325 mesh)	Te	Alfa Aesar	99.99	127.60	-
Tetrachloroethylene	TCE	Aldrich	99.999	15.82	1.622
Toluene (anhydrous)	Tol	Aldrich	99.8	92.14	0.867
Trioctylphosphine	TOP	Aldrich	97	370.64	0.831
Deionised H_2O purified by purifier in the laboratory.					

PbTe Synthesis

Precursor preparation

For preparing a standard synthesis, which yields ~5.5 nm PbTe NCs, the precursors described in the next section were used. In order to keep the text readable, only standard units of materials are provided in this description. In the Supporting Information 1, more detailed information about the molar ratios between precursors can be found.

Pb-precursor

In a fumehood, 1.138 g lead acetate trihydrate ($Pb(Ac)_2\ 3H_2O$), 3.3 ml of oleic acid and 8 ml of octadecene were combined in a three-neck flask. The three-neck flask was then connected to a Schlenkline, put under vacuum and flushed with nitrogen (N_2) in order to get rid of O_2 in the reaction atmosphere. This cycle was repeated three times. After flushing, the mixture was put under vacuum again and the temperature was slowly increased to 130°C. At this temperature the solid $Pb(Ac)_2\ 3H_2O$ separates and the newly formed water and acetate leave the mixture in gaseous form. The temperature was maintained at 130 °C for at least three hours, until no bubbling was visible anymore.

Te-precursor

The tellurium precursor was completely prepared in the glovebox because of its sensitivity to oxygen. In the glovebox, 0.194 g of tellurium was combined with 3 ml of trioctylphosphine (TOP) and stirred at ~90°C, until the solution was completely transparent and yellow.

Hot-injection method

The synthesis of Lead Telluride (PbTe) nanocrystals (NC) was done with the hot-injection method as described by Murray et al[60]. This synthesis allows differently sized monodisperse PbTe NCs to be formed through varying reaction time, injection temperature and OA:Pb ratio[60,61]. The previously prepared Pb-oleate is first heated to 170°C in a 3-necked flask in a schlenk line, after which the TOP-Te is rapidly injected under vigorous stirring (figure 5). Upon injection, the solution immediately turns deep black. It is of key importance that the injection happens quickly and without stopping the stirring, in order to avoid concentration gradients in the mixture. After four minutes the growth process was quenched by quickly injecting 3 ml of hexane into the solution. The ensuing effect was a reduction of the reaction temperature, but also a dilution of the solution below supersaturation levels. Further cooling of the reaction was achieved by placing the flask in a water bath or blowing cool air onto the flask.

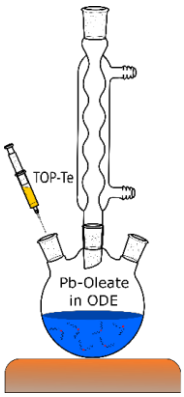

Figure 8. Schematic representation of the hot-inejction method. The Te-precursor is quickly injected into the Pb-oleate mixture at 170-degrees.

Once the solution had cooled down to room temperature, the PbTe NCs were washed inside a glovebox. The first step was to add water free ethanol with an approximate ratio of 2/3 to the original volume. If the system turned from oily black to dark grey and flaky, it was sufficiently destabilized. The samples were then placed in a centrifuge and rotated at 2900 RPM for 10 minutes. The precipitate was then separated from the supernatant and redispersed in hexane. This washing cycle was repeated 5 times for every sample in order to get rid of unwanted reaction products and leftover precursors.

Cation exchange

Cd-Oleate

In a fumehood, 6.26 g Cadmium acetate dihydrate ($Cd(Ac)_2$ $2H_2O$), 17.83 ml of oleic acid and 43.97 ml of ODE were combined in a three-neck flask. The three-neck flask was then connected to a Schlenkline, put under vacuum and flushed with nitrogen (N_2) three times in order to get rid of O_2 in the reaction atmosphere. After flushing, the mixture was put under vacuum again and the temperature was slowly increased to 100°C. At this temperature the solid $Cd(Ac)_2$ $3H_2O$ separates and the newly formed water and acetate leave the mixture in gaseous form. The temperature was maintained at 100 °C for at least three hours, until the evaporation of acetate and water almost completely ceased.

Pb →Cd exchange

The cation exchange from PbTe to CdTe was based on a partial CE process by lambert et al[62]. The first step was to dry 0.8 ml of PbTe NCs dissolved in hexane under high vacuum in a glovebox antechamber. After approximately one hour of drying, the NCs were re-suspended in 2-3 ml of either toluene or ODE. Since these experiments were based on estimates of NC concentration, the amounts are expressed in ml. To this solution, 2 ml of 0.38 M Cd-oleate dissolved in ODE was added. Subsequently, the temperature was increased to 150°C for 4 hours or 17 hours.

Oriented attachment

Square - Short method

The short oriented attachment method was performed at 20°C inside the glovebox mentioned above[57]. In this case, 7.5 µl $3.30E^{-5}$ M solution of PbTe NCs was dried under vacuum and re-dispersed in 800 µl toluene. A small (Ø 27mm) petridish was then filled with 6.5 ml ethylene glycol (EG), thereby creating an outward meniscus. A volume of a 350 µl PbTe suspension was then drop casted on top of the ethylene glycol, which then serves as an immiscible supporting layer. After an hour, a TEM grid was slid gently underneath the surface and scooped upwards to harvest the superstructure. The TEM grid was placed under vacuum to dry any residual ethylene glycol.

Honeycomb method

The honeycomb method has been derived from a procedure designed in the CMI group for PbSe attachment. The NC solution was diluted to circa 0.2 µM in toluene, and then 350 µl wasdropcasted on 6.5ml EG in a small petridish. In a bigger petridish underneath the small one, 2ml toluene is added after which a 350 ml beaker was used to cover both petri dishes. After 5-6 hours the experiment was halted and the sample scooped with a TEM grit.

Characterization

UV-VIS

A Perkin Elmer Lmabda 950 UV/Vis spectrometer was used to conduct absorption measurements in the wavelength range from 300 nm to 2300 nm. The samples were prepared in the glovebox by drying 5-30 µl of PbTe solution under vacuum in absorption cuvettes. The residue was then re-dispersed in 3 ml tetrachloroethylene (TCE) because this solvent does not absorb light in the near infrared spectrum. Before measuring PbTe, a background scan was measured to correct for background noise on the PbTe spectrum.

The information captured in the absorption spectrum was acquired in two different ways. First in the 300-400 nm wavelength region, where the volume corrected absorption was used for further calculations. The second region is the first exciton peak and is different per sample in terms of peak position and width. In order to calibrate for these differences between PbTe samples, the energy integrated area underneath the low energy half of the peak is used.

Transmission electron microscopy (TEM) and energy dispersive x-ray spectrometry (EDX)

Depending on the quality needed for analysis, either the Tecnai 20 or Talos F200X (both 200 keV) electron microscopes were used. If TEM images were only used for size determination Tecnai 20 images provided enough resolution and magnification. In cases where it was necessary to demonstrate lattice fringes within the NCs, the Talos F200X was needed. The latter TEM also has the functionality of EDX.

To prepare a grit containing PbTe NCs, the solution first needed to be diluted. One way was to use a separate vial and dropcast ~100µl of the diluted solution on a tilted area accommodating the TEM grit. Another was to put 5 µl of concentrated PbTe solution next to the grid on the tilted area and dropcast hexane next to it so it covers the grit with NCs. Most of the hexane evaporated within minutes, but it was dried under vacuum so that no leftover hexane remained on the grit.

Inductively coupled plasma optical emission spectrometer (ICP-OES)

The exact concentration of lead in PbTe NCs could be obtained with the Perkin-Elmer Optima 8300 Optical Emission Spectrometer. Before the actual measurements could be performed, the samples and a calibration curve needed to be prepared. The preparation of the calibration curve between 0 and 1 ppm is based on a multi-element solution with known amounts of ion-species. This range of 5 dilutions was inserted into the ICP-OES first, in order to establish the calibration curve.

Pb could not be measured when incorporated in an NC and therefore needed to be dissolved with the use of a strong acid: aqua regia (volume ratio: HNO_3 1: 3 HCL) was used. The next step was to dilute the samples to the region between 0 and 1 ppm. This was done by adding 5% HNO_3 solution, taking an aliquot of this solution and adding more 5% HNO_3. Based on estimates of the concentration in the original sample, one could obtain the right concentration. If the values were too high or low, another dilution had to be made from the previous dilution.

The outcome of ICP-OES consists of several spectral lines for Pb, one of which is chosen based on the quality of the results. This is evaluated by looking at the signal to noise ratio, the intensity, the relative sensitivity and whether the signal overlaps with that of another element. The wavelength chosen for Pb is 283.306 nm.

H-Nuclear magnetic resonance

All NMR measurements were conducted with H-NMR measurements. For NMR measurements, 0.5 ml of concentrated PbTe solution was dried and re-dissolved in 0.5 ml deuterated chloroform, which was done in the glovebox. Subsequently, the total volume was placed in an H-NMR sample tube. To this solution, 10 µl of ferrecene was added in order to establish an internal standard. The spectra were then recorded according to the following parameters: 400MHz, $CDCl_3$ at 25 °C with a relaxation delay time of 30s, which is needed for complete relaxation.

Results

PbTe synthesis

The hot-injection method based on the method of Murray et al[60] has proven to be a useful method for making monodisperse PbTe NCs in the in the 3.5-7 nm range, as can be seen in figure 10. Control over the size of the NCs was most easily achieved by varying the OA:Pb ratio in the Pb-precursor or by changing the growth time after injection. Here a higher OA:Pb ratio and longer growth time both lead to larger particles and *vice versa*. Experiments that were conducted with the aim of obtaining larger NCs led to colloidally unstable and polydisperse particles. With the exception of ~12 nm sized cubic structures, which showed no absorption peak and intermediate colloidal stability (Supporting information 1). The difficulty of producing such particles could be a consequence of Ostwald ripening, inherent instability due to prevalence of {100} facets[54] or large Vanderwaals forces.

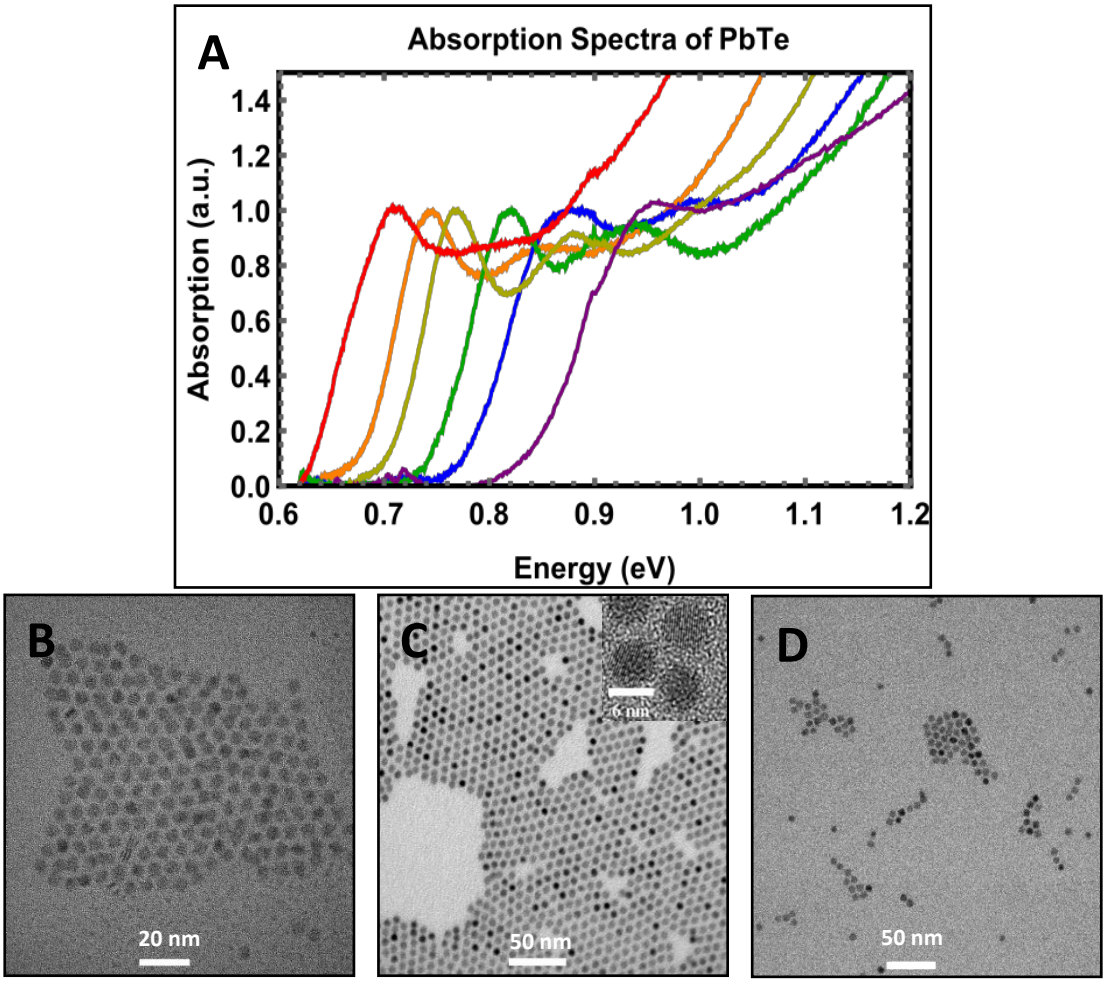

Figure 9. Absorption spectra and TEM images of differently sized NCs. Figure (A) shows normalized absorption spectra measured with UV-VIS absorption spectroscopy of PbTe NCs of 6.85, 5.98, 5.74, 5.2, 4.87 and 4.52 nm from left to right. The shift in peak position is a result of stronger quantum confinement in smaller particles. Figures (B), (C) and (D) show TEM images of small (4.87 nm, σ = 7.8%, blue curve), medium (5.98 nm, σ = 5.5%, orange curve) and large (6.85 nm, σ = 7.7%, red curve) NCs, respectively. The inset in figure (C) is a representative HR-TEM image of the particles and demonstrates the high degree of crystallinity of the PbTe particles.

The as-synthesized PbTe NCs are depicted by the TEM images in figure 1 B,C and D, they seem spherical, despite their cubic rock salt crystal structure. This effect has been studied

extensively and can be explained by the truncation of NCs, which give rise to different facets on the NC surface[56].

When the size dispersion of these NCs is below 10%, the first absorption peak is clearly visible (figure 9A). The second absorption peak is only visible for very narrowly dispersed particles. In general, the indistinct absorption spectrum of PbTe can be assigned to its complex band structure, which gives rise to a number of possible transitions immediately after the first exciton peak[61].

EDX and influence of washing

EDX analysis of the PbTe NCs was carried out in order to establish the ratio between Pb and Te in the NCs. In figure 10, the EDX spectrum of 5.98 nm NCs is shown with a variety of peaks belonging to several elements. The peaks in the spectrum belonging to carbon and copper, are both a result of the materials of which TEM grits are made. Furthermore, the oxygen peak can be explained as both an artefact of the data and as a result of the oxygen atoms present in the surface bound oleate. For the Pb:Te elemental analysis, the L emission lines were used for both Pb and Te. The reason for this choice is that the K-peaks of Te are located at 27 keV, and had very low intensity.

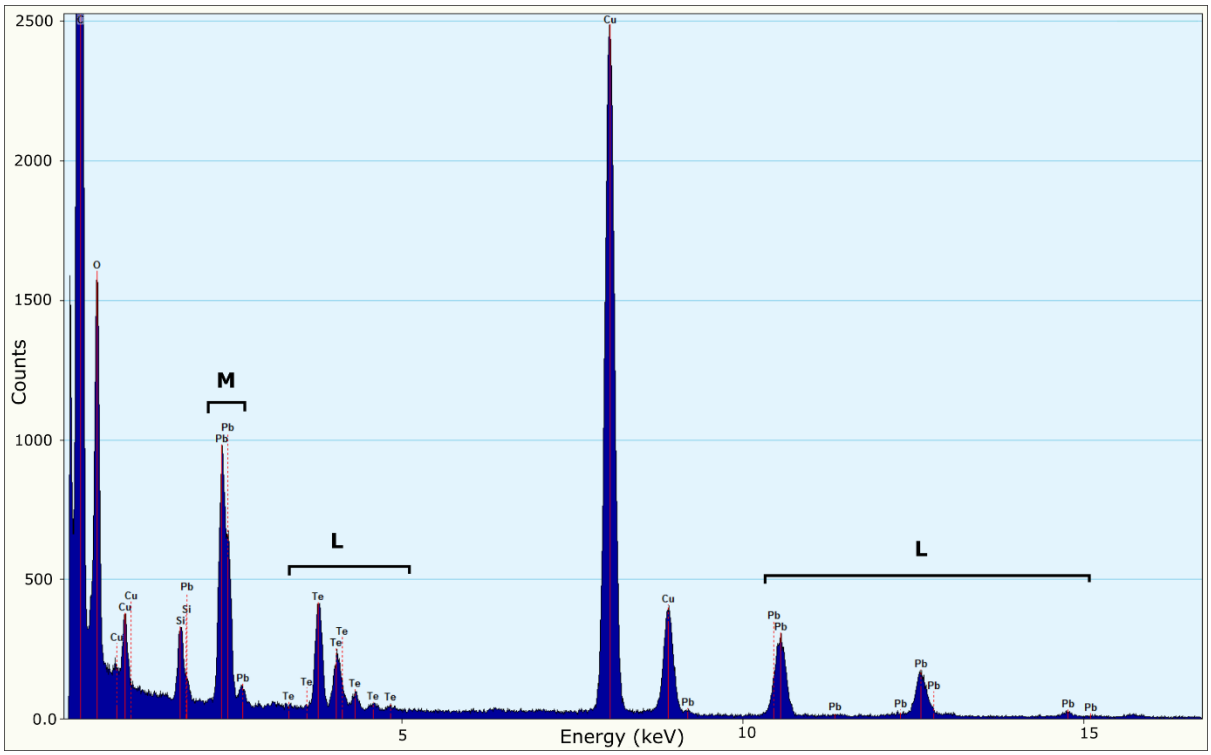

Figure 10. EDX spectrum of 5.98 nm PbTe NCs. For Pb, the L-peak are used for the elemental analsyis. Due to the small peak size of the K-lines of Te (at 27keV) these are discarded and the L-lines are used.

In order to establish whether residual Pb-oleate in solution or attached to NCs could be removed by additional washing steps, EDX was performed on different samples. For two sets of particles, the difference between 3 and 5 washing steps have been measured (table 1). Based on the Pb:Te ratio of small (4.87 nm) and larger (6.85) NCs, 2 additional washing steps seem to affect the atomic ratio of large NCs more than that of smaller NCs. These results do suggest that additional washing steps influence the Pb:Te ratio, whether that is a result of detachment of oleate from the NC surface or removal from solution is unclear.

Furthermore, the general trend that smaller NCs have a higher Pb:Te ratio is not observed in these measurements. This might be due to differences in truncation of the NCs: more NC terminations by {110} and {111} facets means that more ligands can be bound to the steep surface[54]. Unfortunately, HR-TEM measurement could not provide detailed information about the exact shape of the NCs.

Table 1. Influence of washing steps on the atomic ratio in PbTe NCs.

NC Size	Washing steps	Pb (L) atomic %	Te (L) atomic %	Atomic Ratio
4.87 ± 7.7%	3	54.27	45.72	1.18
	5	53.87	46.13	1.16
5.74 ± 6.7%	6	55.24	44.75	1.24
5.98 ± 5.5%	6	54.09	45.90	1.18
6.85 ± 7.8%	3	54.61	45.38	1.20
	5	53.59	46.40	1.15

Ligand coverage

H-NMR analysis provides a measure for the presence of Pb-oleate in solution and bound to the NC surface. Pb-oleate dissolved in the solution can be spotted qualitatively by looking at the vinyl-peak (figure 11, peak X): a Gaussian distribution indicates that all Pb-oleate is bound to the NC surface. If there is still Pb-oleate in solution, the small size causes a faster tumbling speed[27,63]. Because this sharp peak is not observed in the PbTe spectra it is established that all oleate is bound to the PbTe.

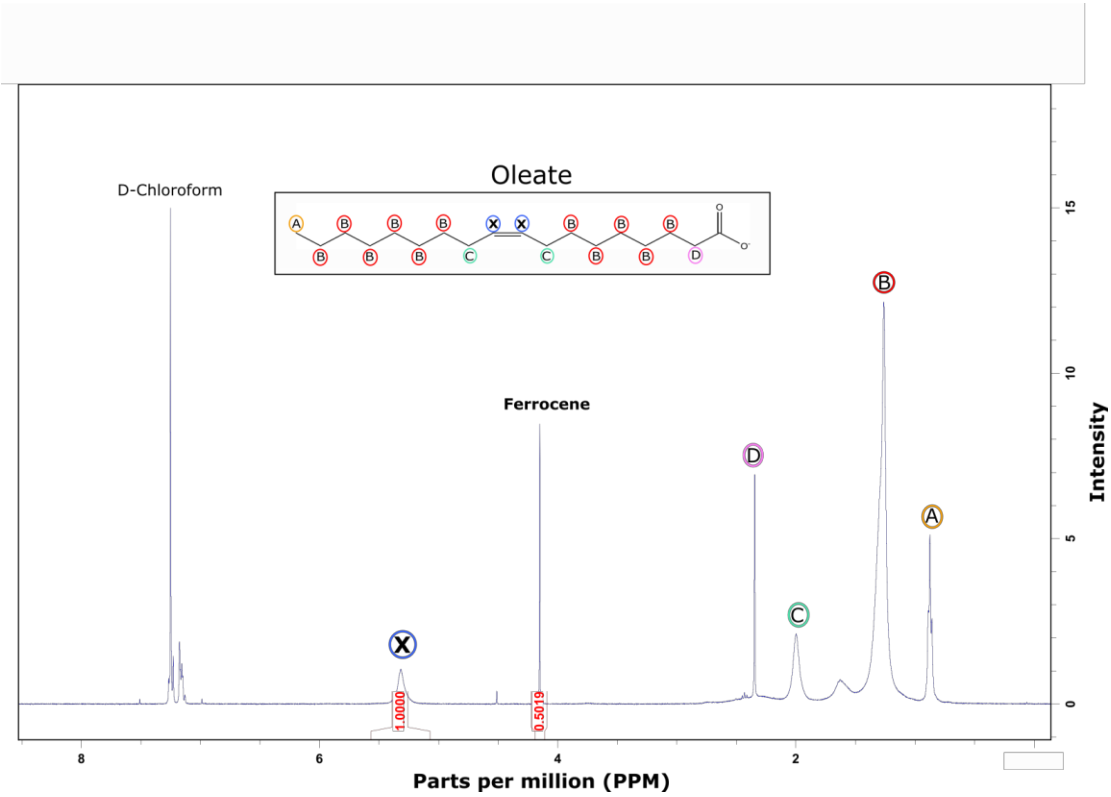

Figure 11. The H-NMR spectrum of 5.98 nm PbTe dissolved in d-chloroform.

The H-NMR spectrum also provides the possibility of calculating the amount of oleate molecules bound to the NC surface, assuming a spherical particle. This was done by adding a known amount of ferrocene solution into the sample tube before analsyis. This molecule contains 10 C-H bonds, which provide a separate peak at 4.15 PPM. This is compared with the 2 vinyl C-H bonds found in oleate at 5.4 PPM. Since the concentration of ferrocene is known, the integrals of both can be compared as in the following equation:

$$[Oleate] = \frac{I_{vinyl}}{I_{Ferrocene}} * \frac{10}{2} * [Ferrocene]$$

The results of the oleate density is displayed in table 2.

Table 2. Oleate density for differently sized NCs based on H-NMR analysis.

Size (nm)	4.54	4.87	5.74	5.77	5.98	6.69	6.85	6.95
Oleate density (oleate/nm^2)	3.35	6.20	6.87	5.54	5.23	3.58	4.07	4.64

The displayed values are roughly twice as high than those found for comparable PbSe oleate NCs[56]. It seems unlikely that PbTe NCs can sustain much higher amounts of oleate molecules. At this point, the only possible explanation could be that over time the concentration in the ferrocene solution has changed. New measurements need to be conducted on these samples to determine whether it is the result of a systematic error. In oriented attachment experiments, the latter is assumed so that the relative densities can be used.

Sizing curve

The band gap of bulk PbTe is calculated to be 0.313 eV, which makes it a narrow band semiconductor material with a very large exciton Bohr radius (150nm)[64]. This combination of properties allowed PbTe absorption to be tuned over the electromagnetic spectrum from 1.23 to 0.79 ev, which covers a large part of the near infrared spectrum. The black dots in figure 12 represent the size as measured by TEM (x-axis) and peak position of the first exciton (y-axis) of the as-synthesized PbTe NCs. In the supporting information 2, the graph is shown with errors bars for the size.

In the search for an appropriate fit for this data, experimental and theoretical results from PbSe and PbS mainly served as guidance. For PbSe, tight-binding calculations agreed well with experimental data, indicating a predominantly 1/d relation between bandgap and size[30]. This is reasoned to be a result of the mostly linear energy dispersion around the gap, even though the small region around the gap is parabolic[29]. The same line of thought can be applied to PbTe, which has a more anisotropic band structure, but does have a similar linear band structure near the gap[65]. The following fit describes the red line in figure 12:

$$Eg = 0.376 + \frac{1}{0.422d + 10^{-9}d} \tag{13}$$

Here Eg is the peak position of the NC and d is the NC diameter. An important factor in this equation is the constant 0.376, which is close to the bulk bandgap value. The reason for this is that with increasing NC size, the band gap is expected to become the same as for bulk PbTe.

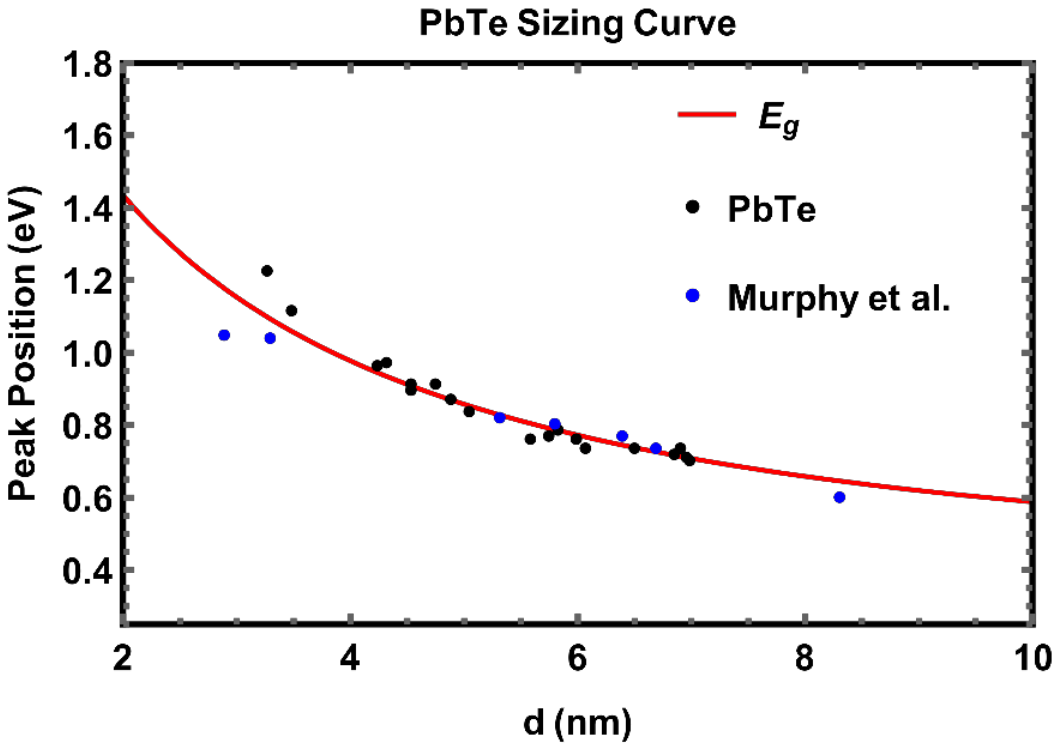

Figure 12. On the x-axis is the NC diameter in nm and on the y-axis is the peak position of the first-exciton of PbTe NCs. The dots represent the measured samples and the red line demonstrates the empirical fit through this data. The small amount of data from both Murphy et al and Urban et al have also been plotted and fitted, and deviate significantly from the experimental plot from this research.

The experimental results of the PbTe syntheses are also compared to previous work (figure 12). Results from Murphy *et al.* show a good agreement with experimental results in the 4-7 nm range[61]. For smaller particles a discrepancy is observed, which might be a result of the increased difficulty of synthesising and measuring such particles. In the paper from Urban *et al.* on the other hand, the peak position of similarly sized particles is significantly lower in energy than found in this research[60]. It is ruled out that in the paper by Urban *et al.* an outer amorphous layer increases quantum confinement effects, since they have included HR-TEM images that show completely crystalline NCs. However, if their data is fitted with the same function, the fit converges at a higher energy. The functions describing the fits for the data gathered from the two papers are as follows:

$$Urban\ et\ al: Eg = 0.44 + \frac{1}{0.957d} \tag{14}$$

In order to further examine the validity of the fit, the empirical relations for PbS and PbSe provide additional insight. The bulk bandgap of PbS is 0.41 eV and for PbSe the bulk bandgap is 0.28 eV. The asymptotes of both sizing curve fits show good agreement with these bulk values:

$$PbS^{30}: Eg = 0.41 + \frac{1}{0.283d + 0.0252d^2} \tag{15}$$

$$PbSe^{32}: Eg = 0.278 + \frac{1}{0.045 + 0.209d + 0.016d^2} \quad (16)$$

Comparing these relations the experimentally determined relation for PbTe, deviating features are the inverse quadratic parameter and the bulk bandgap value. Given the good fit of the datapoints between 4-7 nm, this is not very influential for size-determinations in that size range. However, if the size of smaller or larger particles needs to be accurately determined additional data in those ranges is necessary. Especially since the curvature of the fit is heavily reliant on the values in those margins.

Cation exchange

The cation exchange of Pb for Cd in PbTe NCs has been conducted with preservation of the original size and form (figure 13A,C), based on the methods used by Lambert *et al*[62]. In figure 13 the process is demonstrated for a CE carried out in toluene as the solvent. Image 13B provides a clear indication that the exchange process for the most part happens within an hour, since the characteristic PbTe absorption peak has completely vanished. Over time, the peaks become more pronounced, which is most likely due to the increased exchange of Pb for Cd. Another important thing to note is the small absorption redshift with increasing redshift (figure 13B), which is a result of the increasingly confined PbTe core[66]. If one compares the absorption spectra obtained from this sample to a monodisperse CdTe NCs, the difference between offsets is apparent: the elevated area from 0.8 – 1.7 eV seen in figure 13B is absent from the synthesized CdTe NCs[67].

This difference can be explained by the presence of leftover PbTe in the core of the NCs and residual PbTe in solution. The former is a result of the difficult exchange due to unfavourable CE conditions as a result of lattice formation enthalpies of PbTe and CdTe[47,68]. This is confirmed by a previous report on cation exchange from PbTe to CdTe, where the inner PbTe core had a different shape in every NC, indicative of an anisotropic exchange reaction[46]. The latter explanation is based mainly on the observation that the vials containing the exchanged produce, even after repeated washing cycles, remained murky. These undesired side products also made atomic ratio measurements with EDX unreliable measures for the Pb:Cd ratio.

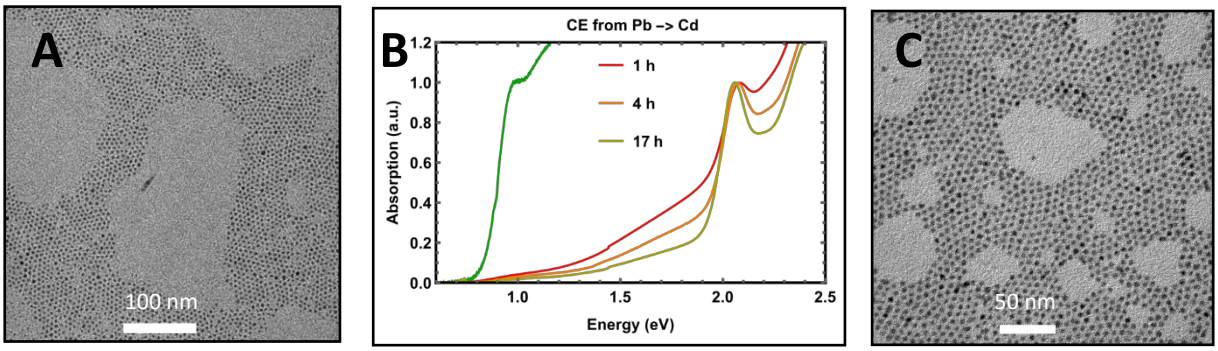

Figure 13. In figure A the 4.4 nm ± 8% sized PbTe particles are depicted, which corresponds to the green absorption curve seen in (B). Aliquots taken at different time intervals show that the exchange from PbTe to CdTe progresses with time and has a small redshift of the first absorption peak as a result. Figure (C) shows TEM images of the particles after 17 hours, which still have the same size and shape as the initial particles.

When the solvent in which the exchange was conducted was changed to ODE instead of toluene, the results improve considerably (figure 14). The main reason for switching from toluene to ODE is that the reaction temperature of 150°C causes some of the toluene to evaporate. An explanation for the improved exchange is that the constant reaction volume in

ODE ensures that the oleate concentration remains constant. In the case that the reaction volume decreases and the oleate concentration increases during the exchange, the equilibrium will shift. This means that due to the increasingly high concentration of Pb-oleate, exchange process can happen forward and backward.

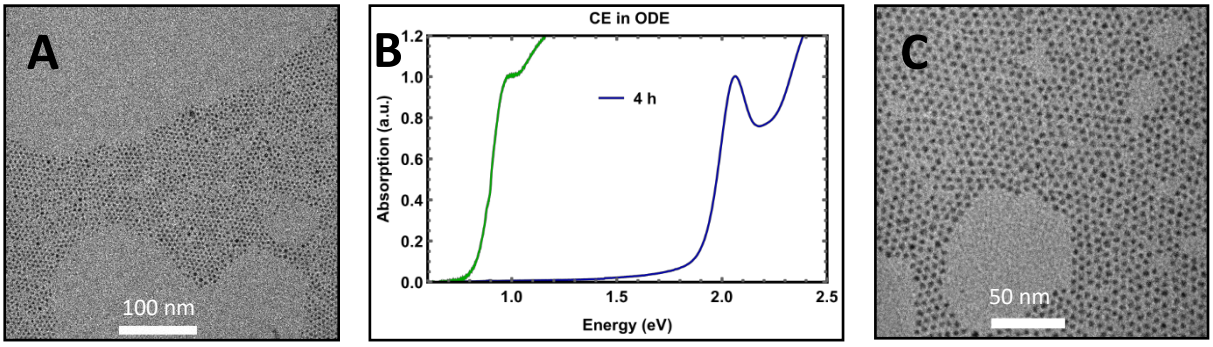

Figure 14. With the same set as particles as described in figure 2, another CE was performed in the solvent ODE. In figure (B), the transition in absorption spectrum from (green) PbTe to blue (CdTe) is demonstrated. In comparison with the CE described above, the use of ODE as solvent gives a more distinct CdTe peak. The TEM image in (C) depicts the CdTe particles after cation exchange with the same size and shape.

An important barrier for performing CE on PbTe NCs is that the concentration is unknown. This requires that for every batch of particles that is made, a new estimate of the Pb:Cd ratio needs be tested. Furthermore, it reduces the experiments reproducibility because there is no way of exactly repeating the measurements. In light of these problems, it was decided to halt CE experiments and continue with finding an accurate way to determine the PbTe concentration in solution.

Quantifying light absorption

NC concentration

The sample purity and NC size and elemtal ratio is determined with the combined use of H-NMR , TEM image analysis and EDX for 8 samples with different sizes. As discussed earlier, all particles are washed 5-6 times with ethanol in order to get rid of all unreacted precursors. In accordance with a paper from Peters *et al.,* H-NMR is used to establish that all oleate is bound to the NC surface[56]. To determine the size of the quantum dots, approximately 300 particles are manually counted with ITEM software (Supporting Information 4). To minimize bias in assessing the particle size, all particles are measured the same way. Finally, EDX analysis is performed to establish the elemental ratio in the PbTe particles. The Pb:Te ratio of 4 samples are measured, after which the average of those values is used for the other particles. The values displayed in table 3 are similar to those reported for PbS and PbSe NCs and demonstrate that PbTe NCs are nonstoichiometric[30,32].

Table 3. Results of TEM image analysis and EDX for differently sized PbTe NCs. [a]Ratio values are estimated by taking the mean of the other results.

NC Size (nm)	σ (%)	Pb (L)		Te (L)		Pb:Te Ratio
		Atomic (%)	Uncertainty (%)	Atomic (%)	Uncertainty (%)	
4.54	10.3	-	-	-	-	1.18[a]
4.87	7.8	53.81	0.15	46.18	0.10	1.17
5.74	6.8	55.24	0.42	44.75	0.31	1.23
5.77	6.4	-	-	-	-	1.18[a]
5.98	5.5	54.09	0.49	45.90	0.30	1.18
6.69	8.5	-	-	-	-	1.18[a]
6.85	7.7	54.61	1.65	45.38	0.95	1.15
6.95	11.7	-	-	-	-	1.18[a]

To determine the PbTe concentration, the data described above is combined with inductive coupled plasma optical emission spectrometry (ICP-OES). Because the ICP-OES can only detect very small amounts of ions, it is necessary to dissolve a known volume of PbTe solution in aqua regia. After all PbTe is dissolved, the solution is further diluted until the appropriate concentration was reached. It is not attempted to measure the concentration of Te^{2-} due to the possible formation of volatile hydrides[69], which can influence the atomic ratio. The measured Pb^{2+} concentrations and their relative standard deviations (RSD) are shown in table 3. Now that the size, elemental ratio and the concentration of the NCs are known, these values can be inserted into equation (4) and (5) to obtain the PbTe concentration (table 4).

Table 4. Results of ICP-OES analysis, absorption measurements at 3.1 eV and [PbTe] calclulations.

Particle size (nm)	[Pb] in mol/L	RSD (%)	N (Atoms/ NC)	[PbTe] (µmol/L)
4.54	0.0173	0.7	1480	43.3
4.87	0.0200	1.8	1827	40.6
5.74	0.0227	2.0	2992	27.5
5.77	0.0294	2.4	3039	35.9
5.98	0.0207	1.8	3383	22.6
6.69	0.0160	4.2	4737	12.5
6.85	0.0275	2.9	5085	20.2
6.95	0.0173	3.1	5311	12.1

The uncertainty for the concentration determination arise from EDX, ICP-OES and the size dispersion. Especially EDX and to a lesser degree ICP-OES have very small error margins and only make a small contribution to the final uncertainty. The uncertainty related to these measurements is estimated to be 3% per NC. The size dispersion of the NCs has a more profound influence given that the standard deviation in the size is several times as high as that of EDX and ICP-OES. This is not taken into account in the calculation of N, but is graphically depicted in the plotting of absorption coefficients in the following sections.

Uncertainty in absorption

Before the concentration of and absorption by PbTe NCs are used to calculate the molar absorption coefficients, the uncertainty in the absorption measurements needs to be discussed. The reason to do this, is that the uncertainty in the y-direction is mainly a result of the uncertainty in the pipettes. They are used for re-dissolving a known amount of PbTe NCs in tetrachloroethylene and are not as reliable as initially thought. To estimate the error originating from this malfunction, the pipette was calibrated using water. Based on the calibrated volumes, new absorption measurements were conducted and showed varying differences in absorption. Since there was not time anymore to redo all absorption measurement, some of the measurements are compared to pervious absorption results. The difference between the values times the combined 3% error from EDX and ICP-OES is used as the vertical uncertainty.

Molar absorption coefficient at bandgap

Analysis of the bandgap starts with integration of the first absorption peak on an energy scale. The first absorption peak is integrated by fitting it with a Gaussian distribution function of the following form:

$$f(eV) = a + be^{-c(eV-pp)^2} \tag{18}$$

Here a is to account for the offset from 0 absorption, b is the height of the center of the peak, c controls the width of the curve, eV gives the measured absorption value at energy E and pp gives the peak position. The next step is to integrate the area under the first half of the absorption peak:

$$I = 2 * \int_{pp-w}^{pp} f(eV)deV \tag{19}$$

The factor 2 doubles the half-width integral, and the integration limit from *pp-w to pp* depends on the width of the curve. The width of the integral is for taking into account size dispersion factors. A Mathematica script that has previously been written by a colleague is used to fit the curve, the integration is then done manually by adapting the integration range.

The energy integrated molar absorption coefficient at the bandgap ε_{gap} is derived from Lambert-Beer's law (equation 4). Figure 15A and table 5 present an overview of the experimental data relating ε_{gap} to NC size. Because in previous work on PbS and PbSe a powerlaw was used to fit the experimental data, a powerlaw without contraints is also fitted to the data for PbTe. At the bandgap, the molar absorption coefficient scales with the following power law:

$$\varepsilon_{gap} = 1.52d^{1.32}\ \frac{meV}{cm\ \mu M} \tag{20}$$

The relation obtained from the data are compared to the energy integrated molar absorption coefficients of PbS and PbSe, and are observed to be very similar[32]. Both materials scale with $d^{1.3}$, but have a prefactor that is slightly higher than that of PbTe. The latter means that PbTe absorbs less light at the bandgap than the other lead chalcogenides. This was experimentally confirmed by the color of the dilution in cuvets as well: PbTe had to be diluted less than PbSe in order to obtain enough absorption for a first absorption peak without too much noise.

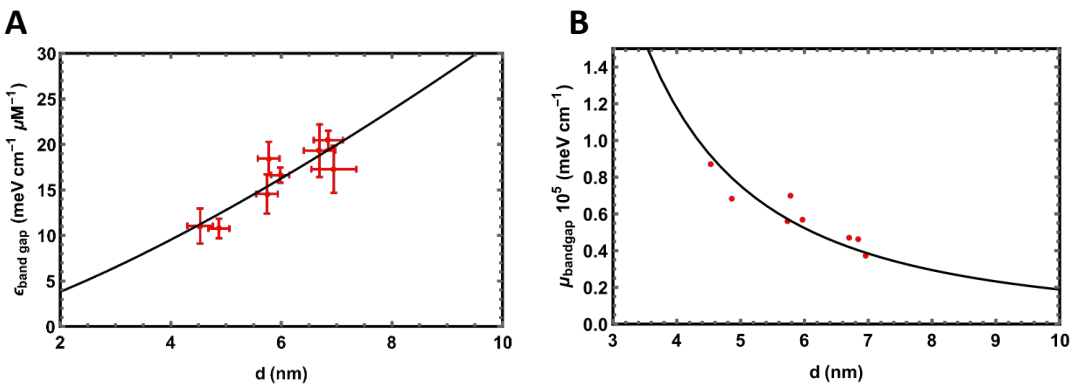

Figure 15. Figure A describes the relation between size and the energy integrated molar absorption coefficient at the band gap. The horizontal errors account for *one* standard deviation of uncertainty on NC size as determined by TEM image analysis. (B) Eequation (21) is used to derive the intrinsic absorption coefficient at the bandgap; the uncertainties are not depicted since they arise directly from the data in graph A.

An additional means of comparison is the energy integrated absorption coefficient μ, which is calculated with the following formula[32]:

$$\mu_{gap} = \frac{6\ Ln(10)\varepsilon_{gap}}{\pi\ d^3\ N_A} = 18.8d^{-2}\ \frac{meV}{cm} \tag{21}$$

The results of the above equation are plotted and fitted in figure 15B. In light of the good agreement of the MACs of PbS, PbSe and PbTe, μ_{gap} also compares nicely to the literature value of PbSe[30]. Here, the errorbars are not plotted because they originate directly from the uncertainty in figure 15A.

Table 5. Experimental data for the determination of the energy integrated molar absorption coefficient at the bandgap.

Size (nm)	Concentration in cuvet (μM)	Energy integrated absorption (meV)	ε_{gap} (meV/μM)	Uncertainty
4.53	0.27	1.60	11.01	1.65
4.87	0.20	1.09	10.76	1.08
5.74	0.16	1.06	14.55	2.16
5.77	0.24	2.22	18.50	1.84
5.98	0.11	0.94	16.62	0.83
6.69	0.08	0.80	19.31	2.90
6.85	0.10	1.04	20.47	1.02
6.95	0.08	0.70	17.29	2.56

Molar absorption coefficient at 3.1 eV

Quantum confinement effects

As mentioned in the literature review on light absorption by NCs, light absorption by NCs is supposedly not influenced by quantum confinement at high energies. To corroborate whether this is the case for PbTe, a simple visual method is applied. Figure 16 presents the absorption spectra of differently size PbTe NCs in a logarithmic plot, which are normalized at 400 nm (3.1eV). Despite the evident influence of quantum confinement effects at longer wavelengths, the spectra converge at shorter wavelengths.

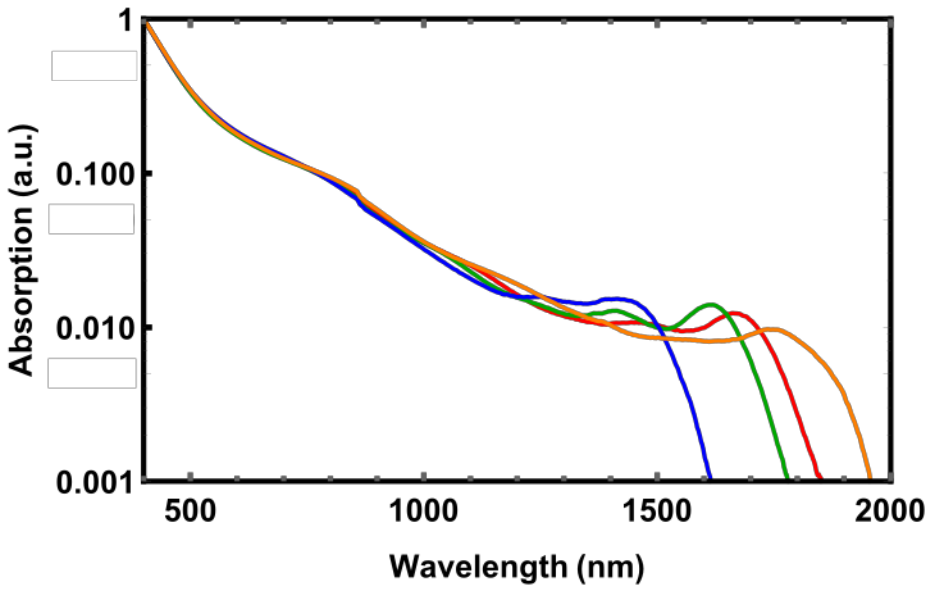

Figure 16. In the logarithmic graph, several absorption spectra of PbTe are plotted. The color-coding relates to the NCs with the following sizes: yellow (6.85 nm), red (5.98 nm), green (5.74 nm) and blue (4.87 nm).

Theoretical absorption coefficient

The theoretical intrinsic absorption coefficient of PbTe NCs provides and additional route to establish whether 3.1 eV is 'quantum confinement free'. The coefficient is calculated and compared with the bulk absorption coefficient. For these calculations the dielectric constant of TCE[70] and the dielectric function of bulk PbTe are needed. Much of the available literature deals with tight-binding caluclations and band-structure approximations[65,71]. The most reliable results for the dielectric function and absorption coefficient of PbTe are measured with spectroscopic ellipsometry (SE), which directly measures both the real and imaginary component of the dielectric function[72]. Based on their data, the local field effect (Figure 17A) and the intrinsic absorption coefficient are determined with equation (9) and (11), respectively. The comparison of the bulk absorption coefficient and the theoretical absorption coefficient are shown in figure 17B.

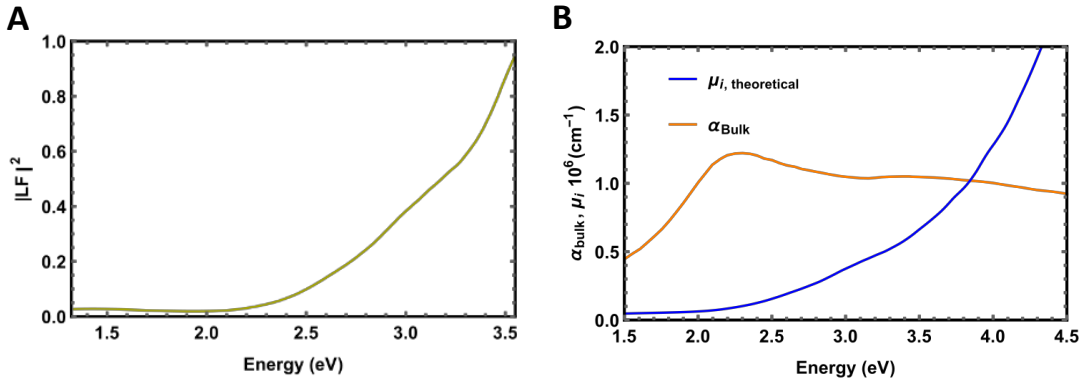

Figure 17. (A) The squared local field effect shows the strong screening effects at lower energies as a result of the local field. (B) The absorption coefficient of bulk PbTe is plotted along with the calculated intrinsic absorption coefficient for nanoconfined PbTe dissolved in tetrachloroethylene.

It can immediately be seen from the graphs in figure 17A and B, that the local field effect strongly influences the absorption coefficient μ_i of nano-sized PbTe. At low energies, the MG effective medium theory predicts that the NCs experience strong dielectric screening from the surrounding solvent. This amounts to a strongly reduced absorption at low energies. A considerable increase of the local field effect also causes the absorption coefficient to increase strongly at high energies.

Data from the theoretical absorption coefficient is compared to experimentally determined absorption coefficients, derived with equation 12. Figure 18 shows both the theoretical constant (blue line) and the experimental data (red points). In the graph, it seems that the experimental data is in rough quantitative agreement with the theoretical data. It is important to note that the measurements are randomly scattered around the theoretical value.

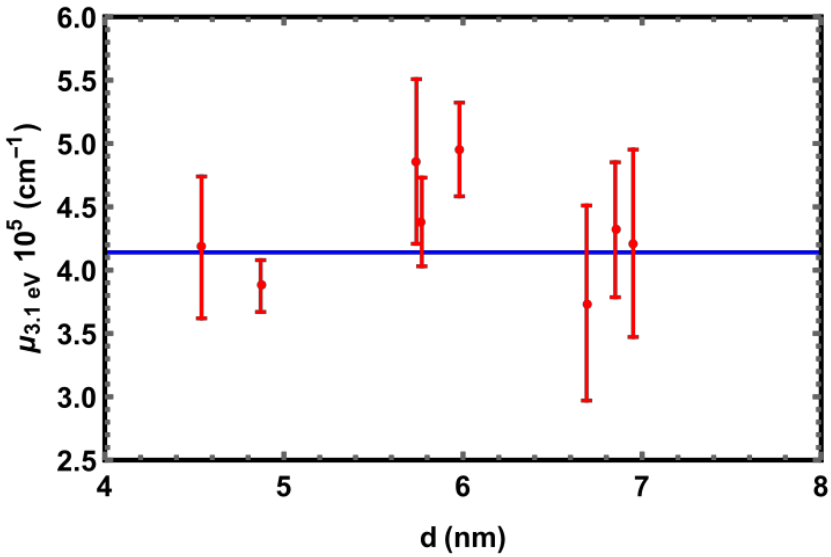

Figure 18. The red dots are the experimental values for the intrinsic absorption coefficient at 3.1 eV and are compared to the theoretical value (blue line). The three measurements whose error bars have no overlap with the

This finding supports that the molar absorption coefficient of PbTe NCs at 3.1 eV is indeed independent of quantum confinement effects. Previous studies have noted that in this case, the molar absorption coefficient scales with the NC volume[30,32,37]. This makes physical sense

since more PbTe will absorb more light. The data derived from Lambert-Beer's law are depicted in figure 19, along with the following fit:

$$\varepsilon_{3.1\,eV} = (0.05846 \pm 0.002)\, d^3\, cm^{-1}\mu M^{-1} \tag{22}$$

The fit shows that the data is in good accordance with literature values. However, the coefficient differs roughly with a factor 2 from the values for PbS and PbSe at 3.1 eV. This difference can be explained with the MG-effective medium theory: for PbTe a roughly twice as strong absorption is predicted than for PbS and PbSe at 3.1 eV.

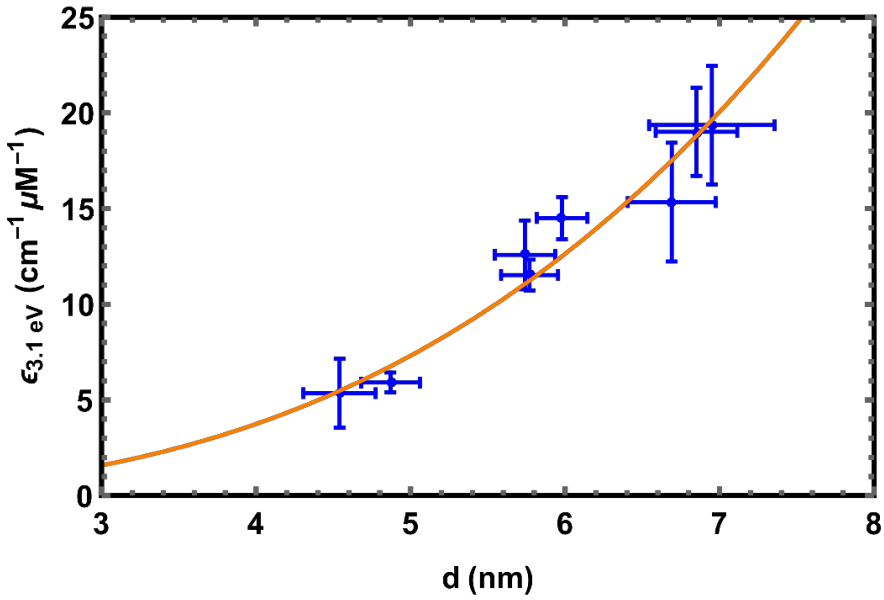

Figure 19. The molar absorption coefficient scales with the NC volume at high energies. The horizontal error bars account for *one* standard deviation of uncertainty on NC size as determined by TEM image analysis.

Table 6. Experimental data for the determination of the molar absorption coefficient at 3.1 eV.

Size	Concentration in cuvet (µM)	Absolute absorption	$\varepsilon_{3.1\ eV}$ (µM^{-1}cm^{-1})	Uncertainty
4.53	0.14	0.773	5.36	1.83
4.87	0.20	1.639	5.91	0.48
5.74	0.13	2.09	12.58	1.81
5.77	0.12	1.379	11.52	0.94
5.98	0.11	1.639	14.50	1.11
6.69	0.04	0.639	15.34	3.18
6.85	0.10	2.09	19.01	2.34
6.95	0.04	0.781	19.36	3.41

Bandgap versus 3.1 eV

A comparison of the two methods yields the molar absorption coefficient as the most reliable way of determining PbTe concentration. Firstly, the cubic fits the data better than the power law relation for ε_{gap}. Another important factor is that the MG mixing rule theory is in

agreement with the experimental data: there are no quantum confinement effects. It is important to note though, that in a report on PbS NCs it is established that quantum confinements do still play a role at high energies, especially for small particles (<4nm). Moreover, the intrinsic absorption coefficient is considered ligand-dependent. These considerations should be taken into account in future work[73].

Oriented Attachment

The oriented attachment of PbTe NCs into square or honeycomb superstructures will be discussed in this chapter.

Square – Influence of size

PbTe NCs of three different sizes were used to perform square oriented attachment to investigate what the effect of NC size is on the formation of superlattices. This is investigated because size influences the degree of truncation: smaller NCs tend to be more truncated than larger NCs. The NC size also influences the defect stability in epitaxially connected superlattices, e.g., larger particles are more prone to structural defects[53]. Given the influence of factors related to size, it might be expected that size affects superlattice formation.

In figure 20 the results for square attachment procedure of PbTe NCs with three different sizes is demonstrated. All dilutions were prepared by drying 4 µl of PbTe solution and dissolving it in 350 µl toluene. After 45 minutes of drying-mediated attachment at room temperature, the samples were scooped with a TEM-grit. Considering the oriented attachment with small particles (figure 20A), it can be seen that there is no order whatsoever. The reason this structure is molten is that the formation of the superstructure happened too fast due to the high reactivity of the small NCs. If the NCs are too small and reactive, attachment is a random process leading to such molten structures.

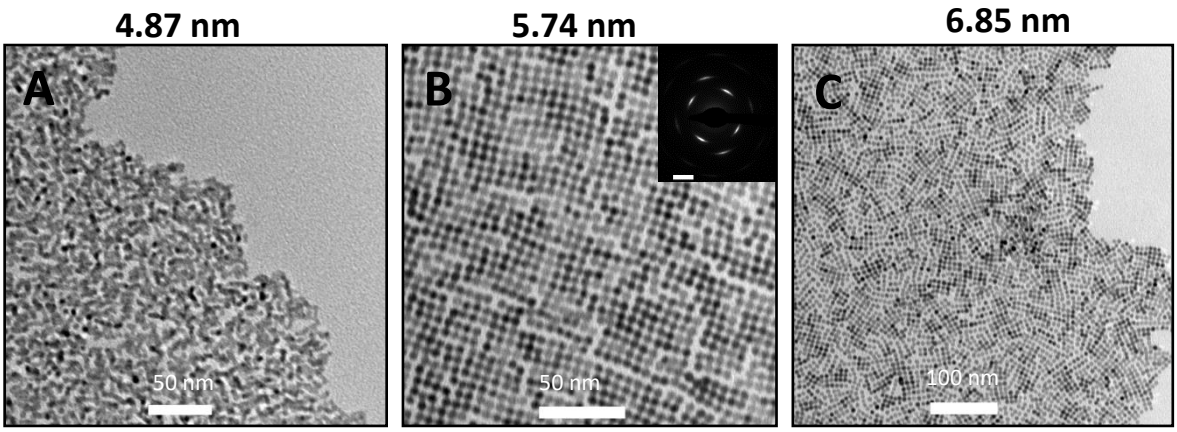

Figure 20. Results of an identical oriented attachment procedure for differently sized NCs. (A) The smallest particles produce a completely molten structure and are not fit to produce square structures. In the medium (B) sized particles micron level square structures are obtained and show sub-optimal short range order. (Inset) The scale bar in the electron diffraction pattern is 5 nm^{-1}. The large (C) particles have a grain like pattern: small square parts and non-attached parts interchange over the long-range.

The results for the medium and larger particles are more promising and produce square superlattices with varying degrees of order. The medium particles have organized into micron-scale superlattices with good long-range periodicity (figure 20B). The electron diffraction patter shown in the inset proves that the long-range order is crystalline to polycrystalline, because the spots are slightly elongated. On the short scale, the structure has semi or non-attached NCs that lead to short-range disorder. This effect is much more pronounced for the

large particles seen in figure 20C. The attachment process seems to have been initiated at several spots at the same time, leading to grain formation. These square grains alternate with small regions of unattached NCs.

Comparing the same oriented attachment procedure for different sizes, medium sized NCs seem to produce the best square superlattices. The 5.74 nm PbTe NCs superlattices are both on the long-and short-range are of better quality than for larger and smaller particles. Both the large and small particles probably have a too fast attachment process, which leads to molten structures and fragmented superlattices respectively. In the case of small particles, the fast attachment could be a result of the inherent instability of the NCs in comparison with larger particles. While for the larger particles a stronger Vanderwaals-interactions can cause the NCs to attach at several spate locations.

Square – ligand density and size dispersion

In this section, the influence of ligand density and size dispersion for different sizes is discussed. The particles are grouped in 3 categories: small (4.53-4.87 nm), medium (5.74-5.98 nm) and large (6.69-6.95 nm). The NCs are grouped because in the previous section, NC size is shown to have a major influence on NC formation. Another important influence is derived from the inherent size distribution of the NCs, which leads to places where superlattices are not connected due to strain[74]. The reason ligand density is also regarded is that a high ligand density is a critical impediment to efficient electronic coupling[52].

As discussed in synthesis section, the absolute values of oleate density/nm^2 appeared to be too high in comparison with prior work. Therefore, a systematic error is assumed in the results from these measurements, and the relative ligand density (RLD) is used. For every size group, the highest ligand density is represented by one, with the other values relative to 1. The relative and absolute oleate densities/nm^2 are listed per size group in table 5. For every NC, the concentration of PbTe in toluene is also provided in table 1.

Table 7. Absolute and relative oleate densities / nm^2 for differently sized NCs.

Size group	Small NCs		Medium NCs			Large NCs		
Size (nm)	4.87	4.53	5.74	5.77	5.98	6.95	6.85	6.69
Relative oleate density	1	0.53	1	0.81	0.76	1	0.87	0.77
Absolute oleate density (oleate/nm^2)	6.2	3.34	6.87	5.54	5.23	4.64	4.06	3.58
[PbTe] µM	0.20	0.22	0.14	0.18	0.13	0.06	0.10	0.06

In figure 21A and B, TEM images are shown of small NCs after a regular square attachment procedure. Contrary to what one would expect, the particles with smaller size, lower ligand density and wider size distribution produce a less molten superlattice (figure 21B). Given these conditions, the particles should be more reactive and therefore produce a more molten structure. Although both structures lack any order this difference is difficult to explain. A reason for this disparity might be a difference in temperature in the glovebox during the attachment procedure.

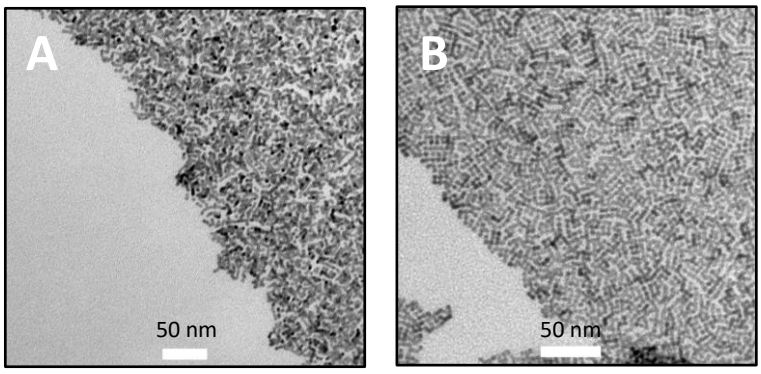

4.87 nm ± 7.8%

RLD = 1

4.53 nm ± 10.3%

RLD = 0.53

Figure 21. TEM images of small PbTe NCs after a square attachment procedure. Both NCs produce molten structures.

Results for the medium sized particles are depicted in figure 22, and follow a more logical pattern according to literature. The particles with the highest ligand density in figure 22 A and B, have the highest superlattice quality. A small difference between the superlattices in figure 22 A and B is that the latter has thicker necking structures, which could be a result of the lower RLD: less ligands have to be displaced for the necking to take place. The superstructure in figure 22C is composed of small areas with square structures with different orientations. Although the RLD is only slightly lower, it might cause the NCs to attach more easily due to the reduced barrier.

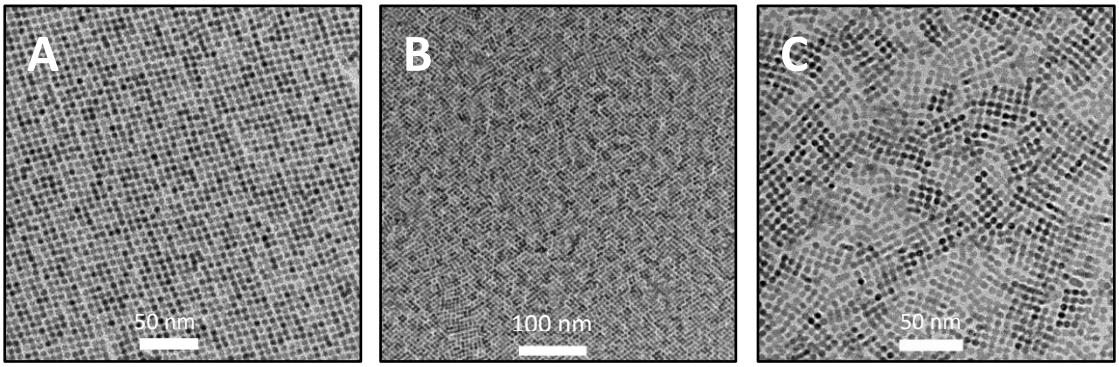

5.74 nm ± 6.8%

RLD = 1

5.77 nm ± 6.4%

RLD = 0.81

5.98 nm ± 5.8%

RLD = 0.76

Figure 22. TEM images for medium sized particles after a square oriented attachment procedure.

Oriented attachment results of the group of larger particles are shown in figure 23. From the TEM figures 23A and C it can be seen that the pattern is linear instead of square. Given that these NCs have the relatively lowest and highest ligand density it seems that the ligand density does not influence the formation of linear or square structures. These NCs do have the widest size dispersion, which can cause more selective attachment, leading to more anisotropic superstructure.

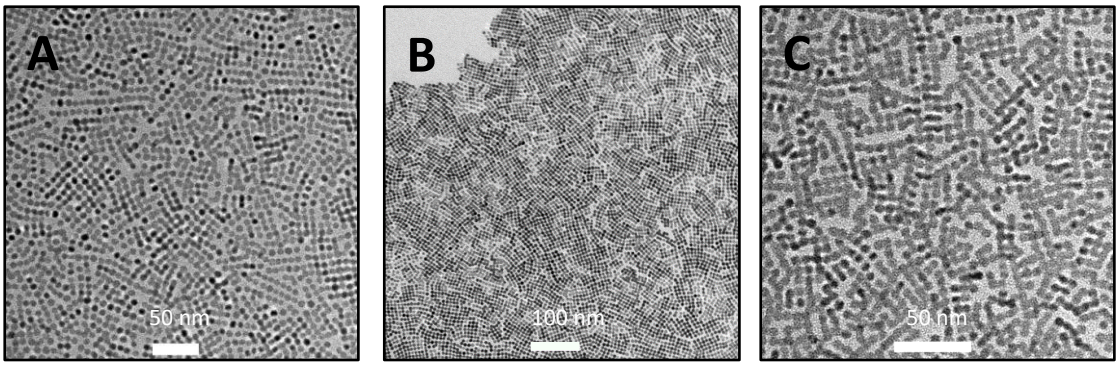

6.95 nm ± 11.7%	6.85 nm ± 7.7%	6.69 nm ± 8.5%
RLD = 1	RLD = 0.87	RLD = 0.77

Figure 23

Square – influence of Pb-oleate

An idea to improve the quality of the square superstructure was to dissolve Pb-oleate in EG. Only very small amounts of Pb-oleate (10^{-6} mol) would dissolve into the EG, which is a result of the long hydrocarbon chain. This addition was supposed to have two effects: firstly, it could increase the physical barrier between the NCs through steric hindrance since Pb-oleat would organize at the EG-toluene interface. Secondly, the equilibrium constant could be shifted which makes it energetically less favourable for Pb-oleate to detach from the NC surface. The goal was to slows down the attachment procedure, which is observed to happen too fast for both large (6.85nm) and small (4.87 nm) NCs.

The attachment procedure is varied in one way: out of 6.5 ml of EG, a certain volume amount of EG contains previously dissolved Pb-oleate. In figure 24A-C, the oriented attachment results for small 4.87 nm NCs are shows for different volumes of EG containing Pb-oleate. Increasing the amount of Pb-oleate in EG affects the degree to which the structures are molten. Using 2 ml of EG containing Pb-oleate, the attachment seems to happen less acute, but still lacks any order. Moreover, the connections between the NCs are very thick and indicate large atomic reorganizations in the NCs. This means that the reactivity of the NCs is still too high for good square attachment. Addition of more Pb-oleate seems to produce similar results with further decreased attachment.

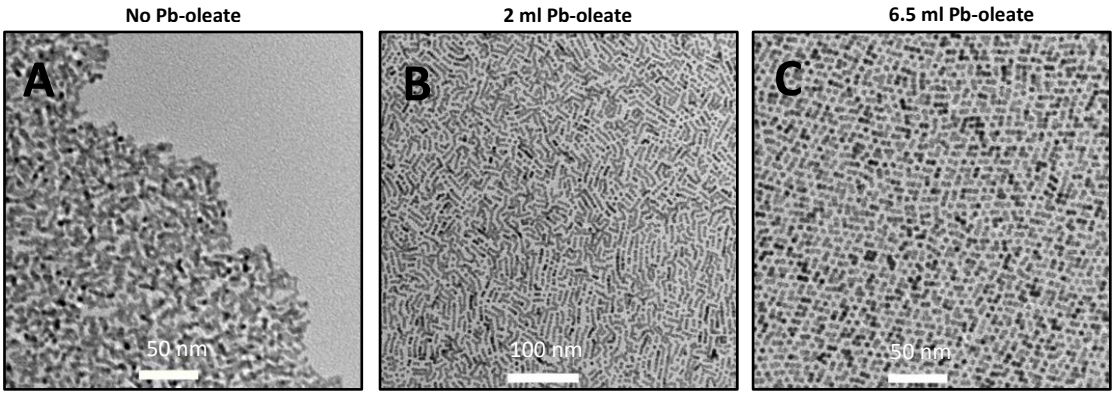

Figure 24. Results of using Pb-oleate in EG with NCs of 4.87 nm. For the small particles a steep increase of EG saturated with Pb-oleate result in less molten structures. When 2 and 6.5 ml of EG saturated with Pb-oleate is used the attachment is random and decreases with increasing addition of Pb-oleate.

The same principle is applied to medium sized (5.74 nm) NCs, although with lower amounts of added Pb-oleate (figure 25). In figure 25C, it can be seen that the addition of 2 ml EG containing Pb-oleate already caused the NCs to stop attaching at all. Instead a close-packed hexagonal lattice is formed with minor particle agglomerations. These results indicate that somewhere in between 0 and 2ml of added Pb-oleate, an intermediate form with an optimal attachment speed is present. These intermediate Pb-oleate containing volumes are shown in figure 25 A and B. The results demonstrate that for increasing volumes, the square superstructure are still obtained, though with lower degrees of order than for attachment without added Pb-oleate.

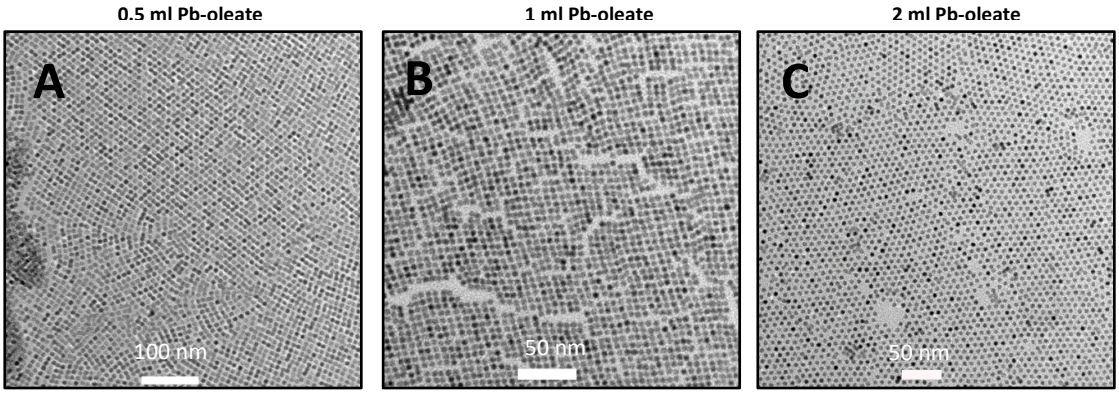

Figure 25. Oriented attachment of 5.74 nm PbTe NCs on EG that is partly saturated with Pb-oleate.

In figure 26 the results for the attachment procedure with large (6.85 nm) PbTe NCs and added Pb-oleate are shown. At the intermediate added volume of 0.5 and 1 ml of Pb-oleate in EG, no clear differences with the original experiment are observed. When the volume is increased to 2ml, something interesting happens: the attachment is halted just enough to stop it from happening midway. In Figure 26C, some patches are organized and attached in a square pattern while others have remained in the hexagonal phase. What probably happened is that at some points the attachment was initiated, which caused the hexagonal structure to contract locally. The resulting strain then causes a rupture between attached and non-attached NCs. Another indication that this process happened at various places, is that differently oriented square structures are observed separately.

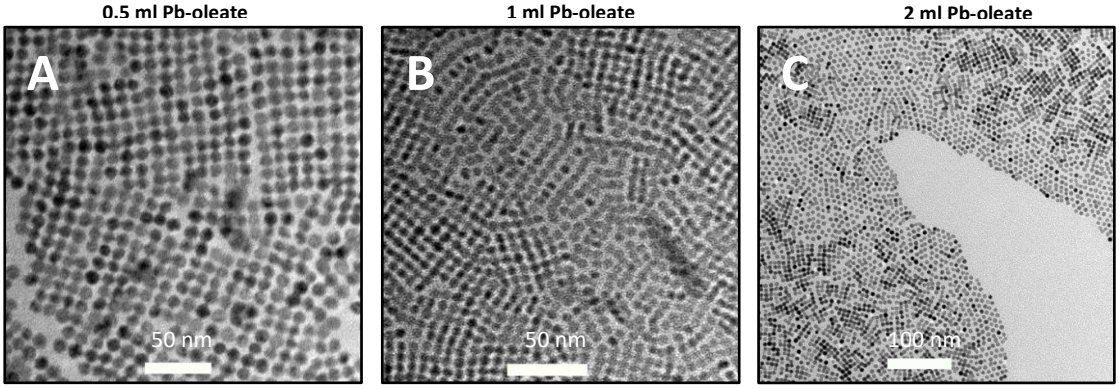

Figure 26. Oriented attachment of 6.85 nm PbTe NCs on EG that is partly saturated with Pb-oleate.

All three sizes indicate that instead of slowing the reaction down, the attachment is hindered by the addition Pb-oleate in EG. For the small particles, it leads to similarly attached structures

although less molten. The medium and large NCs attachment is thwarted at lower added volumes of Pb-oleate, without improvement of the superlattice quality.

Honeycomb – Influence of evaporation time

To achieve honeycomb structures, a method developed in the CMI lab is used. By using a prolonged and controlled evaporation of toluene, the attachment process is slowed down with the aim of obtaining honeycomb superlattices (figure 27B). The idea is that the controlled evaporation causes the NCs to remain longer in the hexagonal phase and eventually attach in that configuration. In comparison with the square method a higher concentration is used, because not a single layer of atoms, but a buckled double layer is expected to form.

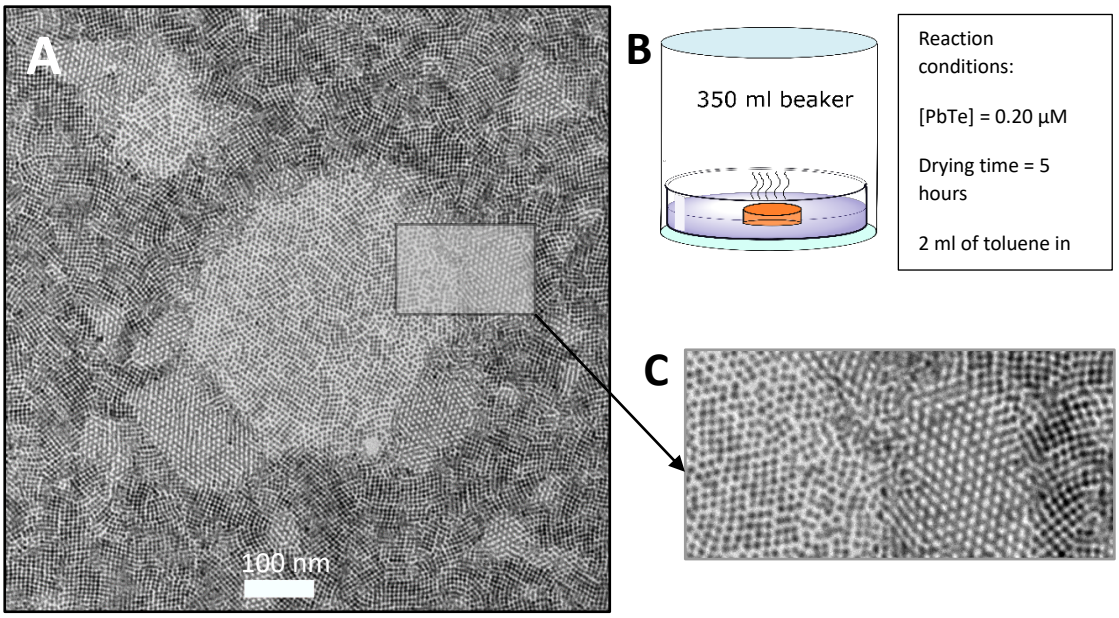

Figure 27. (A) TEM image of attached 5.74 nm PbTe NCs that have been produced with the "long method". These structures are obtained by evaporating the NC solution on EG underneath a 350 ml beaker, with addition toluene in the big petridish. Specific reaction conditions are shown in the textbox. (B) The blue area and zoom-in show a small patch of honeycomb lattice which is enclosed by square and non- attached NCs.

Figure 27A presents the TEM image from the formed superlattice obtained through a 5 hour evaporation process. Small patches with honeycomb geometry are observed and alternate with non-attached NCs and patches with square geometry. There are also variations in layer thickness, as can be seen from the differences in contrast. Going from left to right in picture 27C, first a monolayer of semi-attached NCs is observed. Then a blurry fringe between the monolayer and the honeycomb double layer makes it difficult to distinct a transition geometry. At the right part the square geometry is observed again, this time in a double layer as well.

In comparison with shorter and longer formation time, 5 hours seem to produce the best results. In the case of a shorter drying time the particles do not attach at all (figure 28A), although the low amount of particles indicate erroneous scooping. If the evaporation of toluene is kept on overnight, only molten structures are observed. These results indicate that PbTe NCs have a metastable phase in which it is possible to form honeycomb superlattices.

Conclusion and Outlook

PbTe synthesis

PbTe NCs were synthesized using the hot-injection method based on the procedure of Murphy *et al.*[61] The NCs that were formed with this method, ranged in size from 2.5 -7 nm as measured from TEM images. In order to obtain differently sized particles, variation in the OA:Pb ratio proved to be the most successful route to monodisperse particles. Adjustments of the injection temperature and growing time were also tested, but generally led to less monodisperse particles. It is also important to note, that small particles (2.5-3.5 nm) are more difficult to synthesize and generally have less pronounced absorption peaks and higher polydispersity.

The absorption spectra of PbTe NCs are in general less pronounced than those of PbS and PbSe, due to the complex band structure of PbTe. For very monodisperse particles, a 1st and 2nd exciton peak could be observed. For most particles however, only a distinct 1st absorption peak could be observed.

The effect of repeated washing cycles was investigated, and has a small effect on the stoichiometric ratio of PbTe NCs. Differences in the Pb:Te ration between 3 and 5 washing cycles were observed with EDX. The oleate density/nm^2 was determined using H-NMR, but showed very high ligand densities. New measurements need to be conducted to establish whether this is a systemic error or not.

The first idea for improving PbTe syntheses would be to increase the NC yield. In general, the NC yield remains under 10% with this synthesis method. One could draw inspiration from PbSe, where a tunable library of thioureas can be applied to obtain monodisperse PbSe NCs with a 100% yield and reduced batch-to-batch variability[75]. This does require a lot of practical, trial and error based research on PbTe NCs. A simpler solution might be to apply the addition of diphenylphosphide (DPP) to the Te-precursor[76]. Although it was found in this research that this increases batch-to-batch variability, it does increase the NC yield strongly for PbSe.

Cation exchange

The PbTe-to-CdTe cation exchange procedure has been derived from a partial exchange procedure proposed by Lambert *et al.*[46] The results of this investigation show that after one hour, the characteristic PbTe absorption peak was no longer visible. Instead, an elongated CdTe peak was perceived, which is possibly a result of residual Pb in the core. When the host solvent in which the exchange took place was changed from toluene to ODE, the offset of the CdTe peak began much later. There are two possible reasons for this: first, the toluene evaporates partly at the exchange temperature while ODE remains liquid. The constant reaction volume thus provides more stable conditions. Secondly, the Cd-oleate is dissolved in ODE when added to the PbTe mixture. The fact that both PbTe and Cd-oleate are dissolved in ODE may reduce concentration gradients.

After the cation exchange in both toluene and ODE, the solvents remained murky. Only after repeated washing cycles, there was some improvement, but at that time the solution was extremely diluted. This posed a problem since the resulting CdTe could not be used for further experiments.

To further improve the complete cation exchange from PbTe to CdTe, the use of ODE as solvent is recommended. However, it is very difficult to completely exchange all Pb for Cd

given the unfavourable exchange conditions. If a small residual amount of Pb in the core is deemed acceptable, post-exchange purification is an area that could still be improved.

Sizing curve

A relation between the peak position of the first exciton and the NC size was successfully determined for PbTe. The bandgap scales with 1/d and the asymptote comes close to the bulk bandgap of PbTe. This is slightly different than for other members of the lead chalcogenide family, which scale mostly with 1/d but also with $1/d^2$. Incorporation of PbTe data from previous papers had mixed results: data acquired from Murphy *et al.* overlapped with data from this research, but deviated for NCs in the 2-3 nm range. A consistently lower bandgap value for similarly sized NCs was observed for data from Urban et al., which can not be explained at this point.

Improvements to the sizing curve could be made in two different ways. The first would be to add more measurements to the dataset. This is particularly interesting for small particles, since there is a discrepancy between data from this research and previous work. The second contribution is a theoretical relation between NC size and quantum confinement effects. Tight-binding calculations on PbSe already serve as a frame of reference for an experimentally determined sizing curve[29].

Molar absorption coefficients

The concentration of PbTe NCs dissolved in hexane, was determined with the combined use of TEM, EDX and ICP-OES measurements. EDX measurements demonstrated that PbTe NCs are nonstoichiometric, while the ICP-OES provided the Pb concentration. The combination of these results enabled the calculation of the PbTe concentration, with the assumption that the NCs were spherical.

Based on the PbTe concentration and absorption measurements in TCE, the energy integrated molar absorption coefficient at the bandgap (ε_{gap}) was calculated using Lambert-beer's law. The relation between ε_{gap} and size was in good agreement with literature values for PbSe and and PbS. The comparison of the absorption coefficient μ_{gap} with literature values of PbS and PbSe further corroborated this relation.

The relation between size and the molar absorption coefficient at 3.1 eV ($\varepsilon_{3.1eV}$) was also derived with Lambert-Beer's law and scales with NC volume (d^3). These experiments confirmed that at energies far above the bandgap, quantum confinement effects do not affect light absorption. Moreover, theoretical calculations based on the Maxwell-Garnett-effective medium theory and the dielectric function of bulk PbTe are in rough quantitative agreement with the results.

A limitation to this study is that the amount of data makes the analysis not very robust. Notwithstanding this limitation, the relations for both ε_{gap} and $\varepsilon_{3.1eV}$ do agree with previous work and provide an easy method for obtaining the PbTe concentration. Furthermore, smaller NCs should be included in the analysis of $\varepsilon_{3.1\,eV}$ because a recent report on PbS suggested that both ligands and quantum confinement do play a role[73]. Especially for smaller NCs.

Oriented attachment

The oriented attachment of PbTe NCs has resulted in the formation of square superlattices. To determine the influence of size on square attachment, NCs of 4.87, 5.74 and 6.86 nm were

compared. The smallest NCs appeared to be too reactive to form structured superlattices. Square superlattices composed of 5.74 nm PbTe NCs had micron-range order, but showed small defects on the short-scale. The large NCs do form square superlattices, but the quality is poor due to different attachment initiation sites. This results in separate grains with different square orientations. In conclusion, medium-sized (5.74 nm) NCs are best suited for oriented attachment procedures.

The influence of ligand density and size dispersion on oriented attachment were also investigated. For small particles, seemingly contradictory results surfaced: smaller particles with a lower ligand density and wider size distribution showed marginally better attachment. Whether this was caused by shape factors remains unclear. Medium particles with a narrow size distribution did seem to be affected by the ligand density: lower ligand density led to less order and more strongly attached NCs. In the case of the larger particles, the ligand density does not seem to have a strong influence on attachment. The size dispersion on the other hand, could influence the anisotropy of attachment: for wide size distributions more linear patterns were detected.

Solvation of small amounts of Pb-oleate in EG was also investigated as a factor of influence on the square attachment of 4.87, 5.74 and 6.85 nm NCs. It was hypothesized that the addition of Pb-oleate could slow down the attachment procedure. However, the reaction did not slow down, but was hindered depending and the volume of Pb-oleate containing EG added. This result makes the addition of Pb-oleate to EG no promising addition to the formation procedure of square superlattices.

The formation of honeycomb superlattices was also attempted with 5.74 nm sized NCs. The results show that it is possible to form small honeycomb patches, alternating with single and double square layers. Formation protocols from PbSe cannot be taken over directly for PbTe: the higher reactivity of PbTe causes the formations to lose order at prolonged evaporation times. The most suited evaporation time seems to be around 5 hours, after which a metastable structure containing honeycomb patches is formed.

Regarding the square superlattices, the addition on top of the EG prior to dropcasting the solution is interesting. For PbSe this approach has already yielded good attachment results for long evaporation times. Explorative experiments with this method and PbTe yielded molten structures, which indicates that the formation time also needs to be reduced. Further exploring the influence of ligand density on attachment may also provide new insights about the formation process. For honeycomb superlattices composed of PbTe, the formation time might provide understanding as to why a metastable phase exists at 5 hours.

Acknowledgements

In the past year and a bit I have learned what it means to be a chemist at CMI. After completion of the science and innovation management course I decided that being “in the field” is more interesting than cheering from the sidelines. That idea has been confirmed at CMI, where I have spoken to people working on many different topics. I can see the beauty in so many people striving to add that one extra component to the story, for the greater glory of our continuously evolving world.

That said, I want to thank Daniël Vanmaekelbergh for granting me the opportunity to work at the CMI lab. It is impressive how he, over the course of the years, has build a group that possesses the expertise and creativity to keep approaching the elusive honeycombs from different angles. Given the complexity and diversity of processes involved in the fabrication of this material, such an approach is direly needed.

I also want to thank my daily supervisor Joep Peters. Because of his practical nature and extensive knowledge of chemistry, he never fails to generate new ideas and approaches. I sometimes overthink my results too much, because of which I keep returning to my desk to devise new strategies. From you I learned to change one parameter, go into the lab and check the results. It seems like a simple thing, but sometimes a reality check is all you need!

I want to thank the CMI group members for the warmth and advice on topics ranging from washing particles to the best way of putting on a stocking. The latter refers to my role as Zwarte Piet at the Sinterklaas party of CMI. Thank you Maryam Alimoradi, for thinking of me and Mark when you needed people to throw around pepernoten and have fun. The advice on washing particles and many other things by Tim Prins was always warmly welcomed, especially since I’m too proud sometimes to ask myself. You’ve made up for the millions of times that I was chair less.

My word of thanks would not be complete without mentioning the games of table football and table tennis I have played. I’ve heard many national anthems and I want to thank Luke Chadwick, Mark Magnus, Peter Jacobse, Christiaan Post and all other players for the exciting games downstairs and upstairs.

Lastly, I want to thank all the master students with whom I’ve shared most of my waking hours for over a year. Our talks ranged from the outright bizarre to the deeply touching and everything in between. I’m very glad to have shared this with all of you.

References

1. Walter, P. *et al.* Early use of PbS nanotechnology for an ancient hair dyeing formula. *Nano Lett.* **6,** 2215–2219 (2006).

2. Schmidt, H. M. & Weller, H. Quantum size effects in semiconductor crystallites: Calculation of the energy spectrum for the confined exciton. *Chem. Phys. Lett.* **129,** 615–618 (1986).

3. Donegá, C. de M. Synthesis and properties of colloidal heteronanocrystals. *Chem. Soc. Rev.* **40,** 1512–1546 (2011).

4. Brus, L. E. Electron–electron and electron-hole interactions in small semiconductor crystallites: The size dependence of the lowest excited electronic state. *J. Chem. Phys.* **80,** 4403–4409 (1984).

5. Murray, C. B., Norris, D. J. & Bawendi, M. G. Synthesis and Characterization of Nearly Monodisperse CdE (E = S, Se, Te) Semiconductor Nanocrystallites. *J. Am. Chem. Soc.* **115,** 8706–8715 (1993).

6. Carbone, L. *et al.* Synthesis and micrometer-scale assembly of colloidal CdSe/CdS nanorods prepared by a seeded growth approach. *Nano Lett.* **7,** 2942–2950 (2007).

7. Talapin, D. V., Yu, H., Shevchenko, E. V., Lobo, A. & Murray, C. B. Synthesis of colloidal PbSe/PbS core-shell nanowires and PbS/Au nanowire-nanocrystal heterostructures. *J. Phys. Chem. C* **111,** 14049–14054 (2007).

8. Ithurria, S., Bousquet, G. & Dubertret, B. Continuous transition from 3D to 1D confinement observed during the formation of CdSe nanoplatelets. *J. Am. Chem. Soc.* **133,** 3070–3077 (2011).

9. Berends, A. C. & De Mello Donega, C. Ultrathin One- and Two-Dimensional Colloidal Semiconductor Nanocrystals: Pushing Quantum Confinement to the Limit. *J. Phys. Chem. Lett.* **8,** 4077–4090 (2017).

10. De Mello Donegá, C., Liljeroth, P. & Vanmaekelbergh, D. Physicochemical evaluation of the hot-injection method, a synthesis route for monodisperse nanocrystals. *Small* **1,** 1152–1162 (2005).

11. Niederberger, M. & Cölfen, H. Oriented attachment and mesocrystals: non-classical crystallization mechanisms based on nanoparticle assembly. *Phys. Chem. Chem. Phys.* **8,** 3271–3287 (2006).

12. Cölfen, H. & Antonietti, M. Mesocrystals: inorganic superstructures made by higly parallel crystalizzation and controlled alignment. *Angew Chem Int Ed* **44,** 5576–5591 (2005).

13. Boneschanscher, M. P. *et al.* Long-range orientation and atomic attachment of nanocrystals in 2D honeycomb superlattices. *Science (80-.).* **344,** 1377–1380 (2014).

14. Beugeling, W. *et al.* Topological states in multi-orbital HgTe honeycomb lattices. *Nat. Commun.* **6,** 6316 (2015).

15. Vanmaekelbergh, D. & Delerue, C. Electronic band structure of zinc blende CdSe and

rock salt PbSe semiconductors with silicene-type honeycomb geometry. *IOP Sci.* **2,** (2015).

16. Kalesaki, E. *et al.* Dirac cones, topological edge states, and nontrivial flat bands in two-dimensional semiconductors with a honeycomb nanogeometry. *Phys. Rev. X* **4,** 1–12 (2014).

17. Böhm, M. L. *et al.* Lead telluride quantum dot solar cells displaying external quantum efficiencies exceeding 120%. *Nano Lett.* **15,** 7987–7993 (2015).

18. Harman, T. C., Taylor, P. J., Walsh, M. P., La Forge, B. E. & LaForge, B. E. Quantum dot superlattice thermoelectric materials and devices. *Science* **297,** 2229–32 (2002).

19. Lamer, V. K. & Dinegar, R. H. Theory, Production and Mechanism of Formation of Monodispersed Hydrosols. *J. Am. Chem. Soc.* **72,** 4847–4854 (1950).

20. Yin, Y. & Alivisatos, A. P. Colloidal nanocrystal synthesis and the organic-inorganic interface. *Nature* **437,** 664–670 (2005).

21. Yang, H. W., Luan, W. L., Tu, S. T. & Wang, Z. M. M. Synthesis of nanocrystals via microreaction with temperature gradient: towards separation of nucleation and growth. *Lab Chip* **8,** 451–455 (2008).

22. Baldan, A. Progress in Ostwald ripening theories and their applications in nickel-base super alloys. *J. Mater. Sci.* **37,** 2379–2405 (2002).

23. Kwon, S. G. U. & Hyeon, T. NIC_Colloidal Chemical Synthesis and Formation Kinetics of Uniformly Sized Nanocrystals of. **41,** (2008).

24. Boles, M. A., Ling, D., Hyeon, T. & Talapin, D. V. Erratum: The surface science of nanocrystals (Nature Materials (2016) 15 (141-153)). *Nat. Mater.* **15,** 364 (2016).

25. Anderson, N. C., Hendricks, M. P., Choi, J. J. & Owen, J. S. Ligand exchange and the stoichiometry of metal chalcogenide nanocrystals: Spectroscopic observation of facile metal-carboxylate displacement and binding. *J. Am. Chem. Soc.* **135,** 18536–18548 (2013).

26. Bullen, C. R. & Mulvaney, P. Nucleation and growth kinetics of CdSe nanocrystals in octadecene. *Nano Lett.* **4,** 2303–2307 (2004).

27. Moreels, I., Fritzinger, B., Martins, J. C. & Hens, Z. Surface chemistry of colloidal PbSe nanocrystals. *J. Am. Chem. Soc.* **130,** 15081–15086 (2008).

28. Kovalenko, M. V. *et al.* Prospects of nanoscience with nanocrystals. *ACS Nano* **9,** 1012–1057 (2015).

29. Allan, G. & Delerue, C. Confinement effects in PbSe quantum wells and nanocrystals. *Phys. Rev. B - Condens. Matter Mater. Phys.* **70,** 1–9 (2004).

30. Moreels, I. *et al.* Composition and Size-Dependent Extinction Coefficient of Colloidal PbSe Quantum Dots Composition and Size-Dependent Extinction Coefficient of Colloidal PbSe Quantum Dots. 6101–6106 (2007). doi:10.1021/cm071410q

31. Yu, W. W., Qu, L., Guo, W. & Peng, X. Experimental determination of the extinction coefficient of CdTe, CdSe, and CdS nanocrystals. *Chem. Mater.* **15,** 2854–2860 (2003).

32. Moreels, I. *et al.* Size-Dependent Optical Properties of Colloidal PbS Quantum Dots. **3,** 3023–3030 (2009).

33. Cademartiri, L. *et al.* Size-dependent extinction coefficients of PbS quantum dots. *J. Am. Chem. Soc.* **128,** 10337–10346 (2006).

34. Chopra, K. N. K. n. chopra,' c. **23,** 349–353 (1983).

35. Ekuma, C. E., Singh, D. J., Moreno, J. & Jarrell, M. Optical properties of PbTe and PbSe. *Phys. Rev. B - Condens. Matter Mater. Phys.* **85,** 1–7 (2012).

36. Venkatapathi, S., Dong, B. & Hin, C. Temperature effects on the energy bandgap and conductivity effective masses of charge carriers in lead telluride from first-principles calculations. *J. Appl. Phys.* **116,** (2014).

37. Hens, Z. & Moreels, I. Light absorption by colloidal semiconductor quantum dots. *J. Mater. Chem.* **22,** 10406 (2012).

38. Jasieniak, J., Smith, L., Van Embden, J., Mulvaney, P. & Califano, M. Re-examination of the size-dependent absorption properties of CdSe quantum dots. *J. Phys. Chem. C* **113,** 19468–19474 (2009).

39. Gupta, S., Kershaw, S. V. & Rogach, A. L. 25th anniversary article: Ion exchange in colloidal nanocrystals. *Adv. Mater.* **25,** 6923–6944 (2013).

40. Justo, Y. *et al.* Less Is More . Cation Exchange and the Chemistry of the Nanocrystal Surface. 7948–7957 (2014).

41. De Trizio, L. & Manna, L. Forging colloidal nanostructures via cation exchange reactions. *Chem. Rev.* **116,** 10852–10887 (2016).

42. Parr, R. G. & Pearson, R. G. Absolute Hardness : Companion Parameter to Absolute Electronegativity. 7512–7516 (1983).

43. Rivest, J. B. & Jain, P. K. Cation exchange on the nanoscale: an emerging technique for new material synthesis, device fabrication, and chemical sensing. *Chem. Soc. Rev.* 89–96 (2013). doi:10.1039/c2cs35241a

44. Zhang, C. *et al.* Combination of Cation Exchange and Quantized Ostwald Ripening for Controlling Size Distribution of Lead Chalcogenide Quantum Dots. *Chem. Mater.* acs.chemmater.7b00411 (2017). doi:10.1021/acs.chemmater.7b00411

45. Luther, J. M., Zheng, H., Sadtler, B. & Alivisatos, A. P. Synthesis of PbS nanorods and other ionic nanocrystals of complex morphology by sequential cation exchange reactions. *J. Am. Chem. Soc.* **131,** 16851–16857 (2009).

46. Lambert, K., De Geyter, B., Moreels, I. & Hens, Z. PbTe|CdTe Core|Shell particles by cation exchange, a HR-TEM study. *Chem. Mater.* **21,** 778–780 (2009).

47. Shamsuddin. Thermodynamic investigations of PbTe. *Mat. Res. Bull.* **12,** 7–12 (1977).

48. Schliehe, C. *et al.* Ultrathin PbS sheets by two-dimensional oriented attachment. *Science* **329,** 550–553 (2010).

49. Koh, W. K., Bartnik, A. C., Wise, F. W. & Murray, C. B. Synthesis of monodisperse PbSe nanorods: A case for oriented attachment. *J. Am. Chem. Soc.* **132,** 3909–3913 (2010).

50. Cho, K. S., Talapin, D. V., Gaschler, W. & Murray, C. B. Designing PbSe nanowires and nanorings through oriented attachment of nanoparticles. *J. Am. Chem. Soc.* **127,** 7140–7147 (2005).

51. Evers, W. H. *et al.* Low-dimensional semiconductor superlattices formed by

geometric control over nanocrystal attachment. *Nano Lett.* **13,** 2317–2323 (2013).

52. Whitham, K., Smilgies, D. M. & Hanrath, T. Entropic, Enthalpic, and Kinetic Aspects of Interfacial Nanocrystal Superlattice Assembly and Attachment. *Chem. Mater.* **30,** 54–63 (2018).

53. Ondry, J. C., Hauwiller, M. R. & Alivisatos, A. P. Dynamics and Removal Pathway of Edge Dislocations in Imperfectly Attached PbTe Nanocrystal Pairs; Towards Design Rules for Oriented Attachment. *ACS Nano* acsnano.8b00638 (2018). doi:10.1021/acsnano.8b00638

54. Zherebetskyy, D. *et al.* Hydroxylation of the surface of PbS nanocrystals passivated with oleic acid. *Science (80-.).* **344,** 8–13 (2014).

55. Schapotschnikow, P., Van Huis, M. A., Zandbergen, H. W., Vanmaekelbergh, D. & Vlugt, T. J. H. Morphological transformations and fusion of PbSe nanocrystals studied using atomistic simulations. *Nano Lett.* **10,** 3966–3971 (2010).

56. Peters, J. L. *et al.* Ligand-Induced Shape Transformation of PbSe Nanocrystals. *Chem. Mater.* **29,** 4122–4128 (2017).

57. Geuchies, J. J. *et al.* In situ study of the formation mechanism of two-dimensional superlattices from PbSe nanocrystals. *Nat. Mater.* **1,** 1–8 (2016).

58. Li, D. *et al.* Direction-Specific Interactions Control Crystal Growth by Oriented Attachment. *Science (80-.).* **336,** 1014–1018 (2012).

59. Van Huis, M. A. *et al.* Low-temperature nanocrystal unification through rotations and relaxations probed by in situ transmission electron microscopy. *Nano Lett.* **8,** 3959–3963 (2008).

60. Urban, J. J., Talapin, D. V., Shevchenko, E. V. & Murray, C. B. Self-assembly of PbTe quantum dots into nanocrystal superlattices and glassy films. *J. Am. Chem. Soc.* **128,** 3248–3255 (2006).

61. Murphy, J. E. *et al.* PbTe colloidal nanocrystals: Synthesis, characterization, and multiple exciton generation. *J. Am. Chem. Soc.* **128,** 3241–3247 (2006).

62. Lambert, K., Geyter, B. De, Moreels, I. & Hens, Z. PbTe| CdTe core| shell particles by cation exchange, a HR-TEM study. *Chem. Mater* **21,** 778–780 (2009).

63. Owen, J. The coordination chemistry of nanocrystal surfaces. *Science (80-.).* **347,** 615–616 (2015).

64. Ma, W., Luther, J. M., Zheng, H., Wu, Y. & Alivisatos, A. P. Photovoltaic devices employing ternary PbSxSe1-x nanocrystals. *Nano Lett.* **9,** 1699–1703 (2009).

65. Tudury, G. E., Marquezini, M. V., Ferreira, L. G., Barbosa, L. C. & Cesar, C. L. Effect of band anisotropy on electronic structure of PbS, PbSe, and PbTe quantum dots. *Phys. Rev. B - Condens. Matter Mater. Phys.* **62,** 7357–7364 (2000).

66. Ha, D. H. *et al.* Solid-solid phase transformations induced through cation exchange and strain in 2D heterostructured copper sulfide nanocrystals. *Nano Lett.* **14,** 7090–7099 (2014).

67. Peng, Z. A. & Peng, X. Formation of high-quality CdTe, CdSe, and CdS nanocrystals using CdO as precursor [6]. *J. Am. Chem. Soc.* **123,** 183–184 (2001).

68. Berger, L. I. *Semiconductor materials*. (1996).

69. Filatova, D. G. *et al.* Determination of selenium and cadmium dopants in nanocomposites based on zinc and indium oxides by high resolution continuous source electrothermal atomic absorption spectrometry and inductively coupled plasma mass spectrometry. *J. Anal. Chem.* **71,** 496–499 (2016).

70. Maryott, A. A. & Smith, E. R. *Table of dielectric constants of pure liquids*. (National Bureau of Standars Gaithersburg MD., 1951).

71. Svane, A. *et al.* Quasiparticle self-consistent GW calculations for PbS, PbSe, and PbTe: Band structure and pressure coefficients. *Phys. Rev. B - Condens. Matter Mater. Phys.* **81,** 1–10 (2010).

72. Suzuki, N. & Adachi, S. Optical properties of PbTe. *Jpn. J. Appl. Phys.* **33,** 193–198 (1994).

73. Debellis, D., Gigli, G., ten Brinck, S., Infante, I. & Giansante, C. Quantum-Confined and Enhanced Optical Absorption of Colloidal PbS Quantum Dots at Wavelengths with Expected Bulk Behavior. *Nano Lett.* acs.nanolett.6b05087 (2017). doi:10.1021/acs.nanolett.6b05087

74. Savitzky, B. H. *et al.* Propagation of Structural Disorder in Epitaxially Connected Quantum Dot Solids from Atomic to Micron Scale. *Nano Lett.* **16,** 5714–5718 (2016).

75. Hendricks, M. P., Campos, M. P., Cleveland, G. T., Jen-La Plante, I. & Owen, J. S. A tunable library of substituted thiourea precursors to metal sulfide nanocrystals. *Science (80-.).* **348,** 1226–1230 (2015).

76. Steckel, J. S., Yen, B. K. H., Oertel, D. C. & Bawendi, M. G. On the mechanism of lead chalcogenide nanocrystal formation. *J. Am. Chem. Soc.* **128,** 13032–13033 (2006).

Supporting Information

Supporting Information 1

Large monodisperse NCs

The NCs show no absorption peak and have intermediate colloidal stability. After approximately a week, some sedimentation was visible on the bottom and sides of the vial.

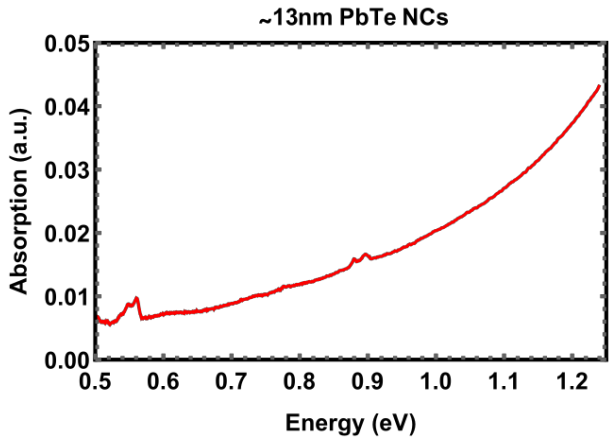

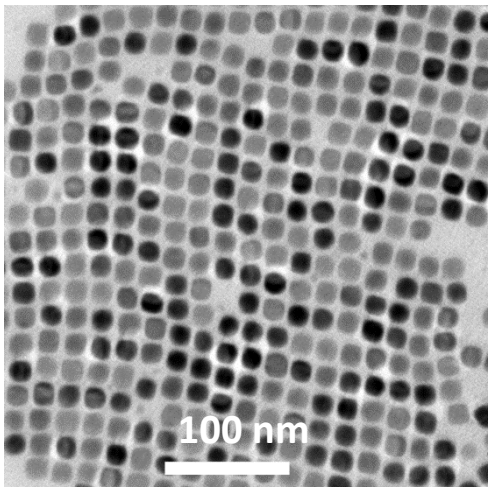

Overview of syntheses

In total, 12 syntheses based on the method of Steckel et al[76] and 14 syntheses based on the method of Murray et al[60] have been performed. In the table below, in the *code* column, S refers to "Steckel synthesis" while M refers to a "Murray synthesis".

Code	Inj. Temp. °C	Growth time (s)	Quenching solvent	Instrument	OA:Pb ratio	Peak (nm)	Note
JW2.2 (S)	180	60	hexane	glovebox	3.63	1600	-broad peak
JW7 (S)	180	90	Hexane	Schlenkline	3.63	x	Stirring stopped
JW8 (S)	180	90	Hexane	Glovebox	3.63	x	Stirring stopped
JW11 (S)	180	90	hexane	Glovebox	3.63	x	
JW14 (S)	180	90	Hexane	Glovebox	3.63	x	Overboiling hexane
JW17 (S)	180	90	Hexane	Glovebox	3.63	x	Overboiling hexane
JW19 (S)	180	60	DFE	Glovebox	3.63	x	
JW21 (S)	180	60	DFE	Glovebox	4.24	x	Bad injection

JW22 (S)	180	60	DFE	Glovebox	5.2	x	
JW24 (S)	180	90	Hexane	Glovebox	3.63	x	
JW26 (S)	180	90	DFE	schlenkline	3.63	x	
JW29 (S)	180	90	ODE	Glovebox	3.63	X	-Square NC
JW30 (M)	170	240	Hexane	Schlenkline	2.67	1790	
JW34 (M)	170	240	hexane	Schlenkline	2.67	1400	Added DPP
JW35 (M)	170	240	Hexane	Schlenkline	2.67	1300	Added DPP
JW36 (M)	170	240	Hexane	Schlenkline	2.67	x	Added dpp White TOPTe
JW41 (M)	170	240	hexane	Schlenkline	2.67	1750	
JW42 (M)	170	240	Hexane	Schlenkline	2.67	1633	2nd exciton peak
JW44 (M)	170	240	Hexane	Schlenkline	5.15	1720	
JW45 (M)	170	240	Hexane	Schlenkline	2	1425	
JW46 (M)	170	240	Hexane	Schlenkline	6.98	x	Bean stopped stirring
JW47 (M)	170	240	Hexane	Schlenkline	6.98	x	Problems Top-te
JW48 (M)	170	240	Hexane	Schlenkline	3	1610	Problems Top-te
JW49 (M)	170	240	Hexane	Schlenkline	6.0	1390	Problems Top-te
JW50 (M)	170	240	Hexane	Schlenkline	2.11	990	Problems Top-te
JW52 (M)	170	240	Hexane	Schlenkline	2.5	1010	Problems Top-te
JW53 (M)	170	240	Hexane	Schlenkline		1100	Problems Top-te
JW54 (M)	180	240	Hexane	Schlenkline	2.67	1620	
JW55 (M)	165	240	hexane	Schlenkline	2.67	1800	
JW56 (M)	170	240	Hexane	Schlenkline	2.67	1830	Less TOP-Te
JW57 (M)	170	60	Hexane	Schlenkline	2.67	1390	

Supporting Information 2

The sizing curve along with 2 standard deviations, thus, 95% of all NCs are in the size range indicated by the error bars.

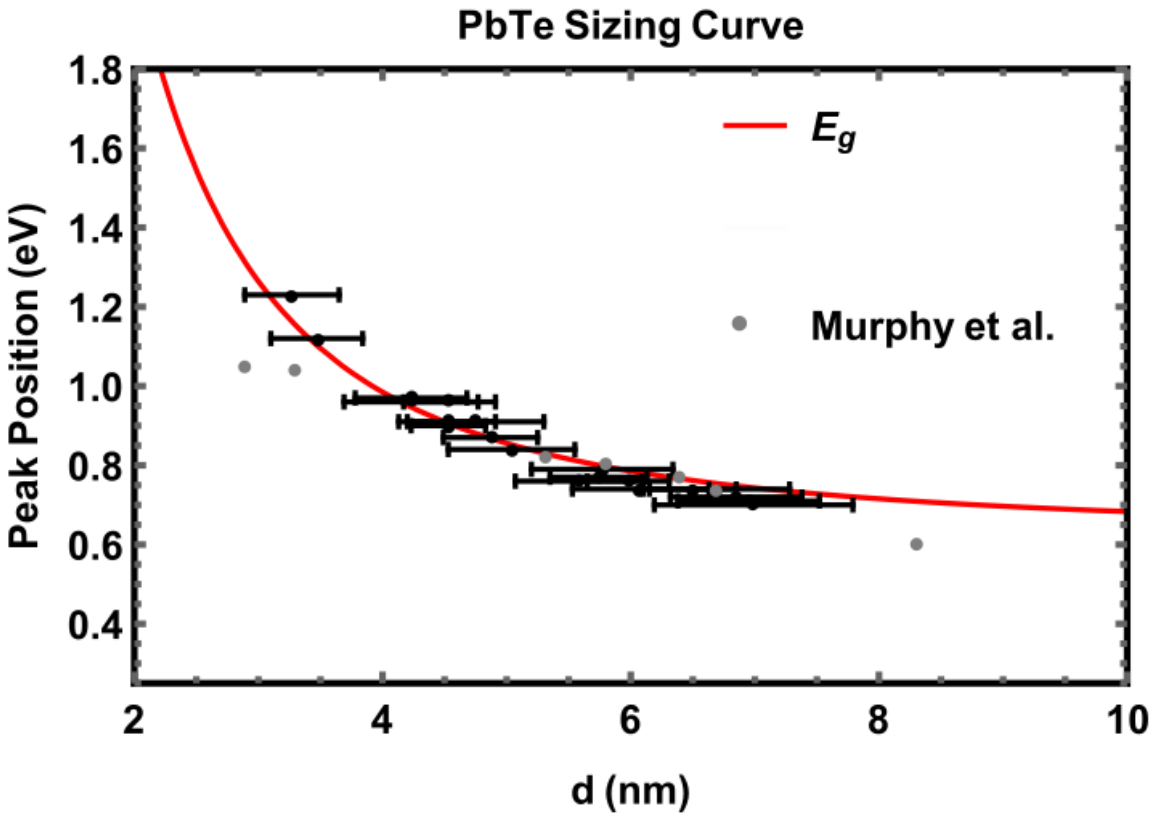

Supporting Information 3

Absorption spectrum of particles in the supernatant of the CE process in toluene. The very dilute sample contained the most distinct absorption spectrum, but could not be used for any follow-up steps.

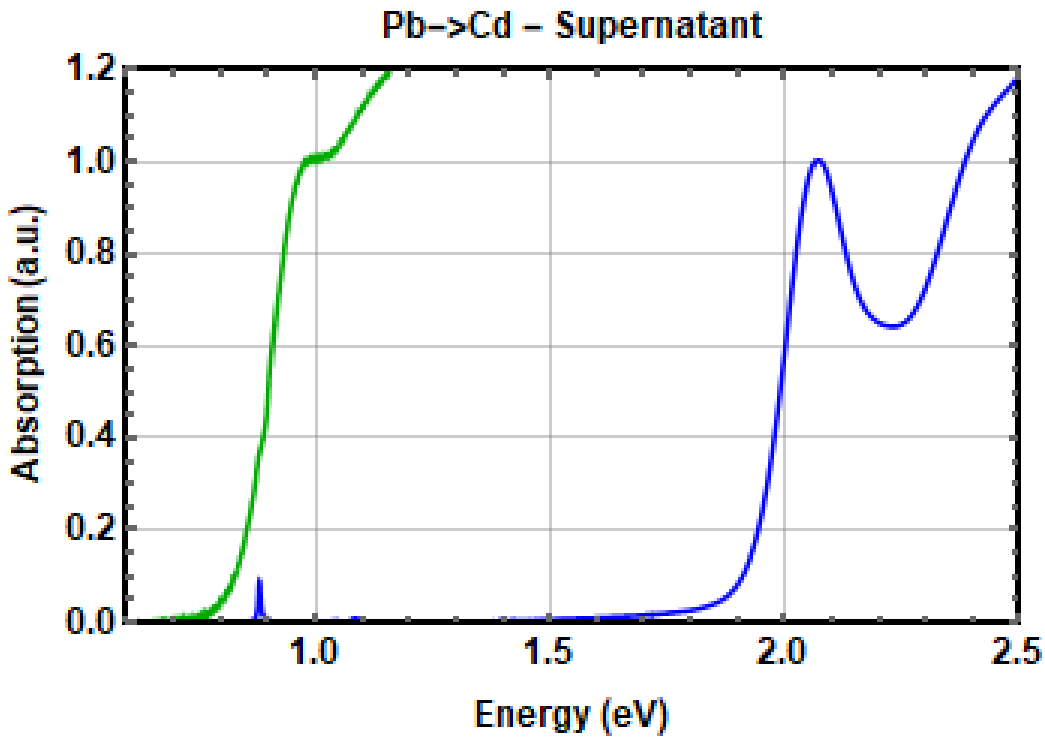

Supporting Information 4

The particle counting software ITEM was used to count the particles. The image would first be calibrated based on the error bar in the lower middle of the image. After the calibration, the NCs were measured solely with the use of horizontal measure bars to reduce bias as much as possible.